http://eprints.gla.ac.uk/135523/

Numerical Simulations on the ERICA Tiltrotor

A. Jimenez Garcia[a], G. N. Barakos[b]

CFD Laboratory, School of Engineering, University of Glasgow, G12 8QQ Glasgow, UK

This paper presents aerodynamic calculations of the model-scale ERICA tiltrotor with high-fidelity computational fluid dynamics. The aim of this work is to assess the capability of the present CFD method in predicting airloads on the tiltrotor at different flight configurations. In this regard, three representative flight configurations of the ERICA were selected, corresponding to aeroplane, transition corridor, and helicopter modes, covering most modes of tiltrotor flight. The rotor blades were fully resolved and the use of a uniform and non-uniform actuator disk was also put forward to quantify the effect of the rotor on the fuselage loads. A fundamental investigation of the effect of the aerodynamic interference between the rotor and wing of the tiltwing aircraft is also shown. The employed CFD method was able to capture the aerodynamics of the different configurations and the overall agreement obtained with the experimental data demonstrates the capability of the present CFD method in accurately predict tiltrotor flows.

Nomenclature

$\bar{Q}$ $\qquad$ = $\bar{Q}$-criterion

ΔP $\qquad$ = jump of pressure across the disk plane, *Pa*

$\mathcal{S}_{\text{ref}}$ $\qquad$ = reference area, m^2

$\mathcal{S}_{\text{rot}}$ $\qquad$ = rotor disk area, m^2

$\boldsymbol{R}$ $\qquad$ = flow equation residual vector

$\boldsymbol{W}$ $\qquad$ = flow solution vector

a_∞ $\qquad$ = freestream speed of sound, *m/s*

C_D $\qquad$ = drag coefficient, $\dfrac{D}{1/2\rho_\infty V_\infty^2 \mathcal{S}_{\text{ref}}}$

C_L $\qquad$ = lift coefficient, $\dfrac{L}{1/2\rho_\infty V_\infty^2 \mathcal{S}_{\text{ref}}}$

C_P $\qquad$ = surface pressure coefficient, $C_P = \dfrac{P - P_\infty}{1/2\rho_\infty V_{\text{ref}}^2}$

[a] PhD Student, CFD Laboratory, School of Engineering. Email: a.jimenez-garcia.1@research.gla.ac.uk

[b] Professor, MAIAA, MRAeS, CFD Laboratory, School of Engineering. Email: George.Barakos@glasgow.ac.uk, corresponding author

L_{ref} = reference length, m

M_{tip} = blade-tip Mach number, $M_{\text{tip}} = \dfrac{V_{\text{tip}}}{a_\infty}$

P = pressure, Pa

P_∞ = freestream pressure, Pa

R = rotor radius, m

T = rotor thrust, N

V_∞ = freestream velocity, m/s

V_{ref} = reference velocity, m/s

V_{tip} = blade-tip velocity, $V_{\text{tip}} = \Omega R$, m/s

C_T = thrust coefficient, $\dfrac{T}{\rho_\infty V_{\text{tip}}^2 \mathcal{S}_{\text{rot}}}$

r = non-dimensional radial coordinate

ΔP^* = non-dimensional ΔP across the disk plane

M_∞ = freestream Mach number, $M_\infty = \dfrac{V_\infty}{a_\infty}$

Re = Reynolds number, $\text{Re} = V_{\text{ref}} L_{\text{ref}} / \nu_\infty$

∞ = freestream value

ref = reference value

tip = blade-tip value

ν_∞ = freestream kinematic viscosity, m/s^2

Ω = rotor rotational speed, rad/s

Ψ = main rotor azimuth, deg

ρ = density, kg/m^3

ρ_∞ = freestream density, kg/m^3

$\theta_{75\%}$ = blade pitch angle at $r = 0.75$, deg

δ_{FU} = fuselage angle of attack

δ_{NAC} = nacelle angle of attack

δ_{TW}	=	tiltable wing angle of attack
μ	=	advance ratio, $\mu = \dfrac{M_\infty}{M_{\text{tip}}}$
(U)RANS	=	(unsteady) Reynolds averaged Navier–Stokes
BVWT	=	Boeing vertical wind tunnel
ALE	=	arbitrary Lagrangian-Eulerian
AC	=	aeroplane configuration
ADYN	=	advanced European tiltrotor dynamics and noise
AoA	=	angle of attack
BILU	=	block incomplete lower-upper
CC	=	corridor configuration
CFD	=	computational fluid dynamics
CFL	=	Courant-Friedrichs-Lewy condition
DART	=	development of an advanced rotor for tiltrotor
DNW-LLF	=	German-Dutch wind tunnels large low-speed facility
ERICA	=	enhanced rotorcraft innovation concept achievement
EU	=	European union
FRB	=	fully resolved blade
GCG	=	generalised conjugate gradient
HC	=	helicopter configuration
HMB	=	helicopter multi-block
MUSCL	=	monotone upstream-centred schemes for conservation laws
NICETRIP	=	novel innovative competitive effective tilt rotor integrated project
NURAD	=	non-uniform rotor actuator disk
ONERA	=	office national d'etudes et de recherches aerospatiales
RK	=	Runge-Kutta

TILTAERO   =   tiltrotor interactional aerodynamics

URAD   =   uniform rotor actuator disk

V/STOL   =   vertical and/or short take-off and landing

I. Introduction

Tiltrotor is a flying vehicle that combines the V/STOL (vertical and/or short take-off and landing) capability of helicopters with the high speed cruise of turbo-prop aircraft. The tiltrotor concept has been intensively studied and investigated during the last sixty years in the United States. For the first time, this technology was successfully demonstrated with the Bell XV-3 in 1955 [1]. In the late 1960s and early 1970s, a major program was jointly launched by the NASA Ames Research Center and Bell Helicopters to develop a new tiltrotor, named XV-15. This hybrid aircraft was used to support the development of a new generation of tiltrotors like the Bell-Boeing V-22 Osprey and the AW609.

Tiltrotor blades must be designed to efficiently operate in helicopter and aeroplane modes, resulting in a compromise blade design with high twist and solidity, along with smaller rotor radius. Hence, the aerodynamic interaction between the rotor and the wings seems to be one of the most important aerodynamic phenomena to affect the design of tiltrotor blades and the overall performance of the aircraft. In this regard, experimental studies carried out by Felker and Light [2] and numerical simulations performed by Potsdam and Strawn [3] investigated the rotor/wing aerodynamic interactions in helicopter mode configuration. To mitigate the strong aerodynamic interaction between rotor and wing of tiltrotors and to reduce the downward force acting on the wings in hover [4], a new design was proposed, where a small part of the wing can be partially rotated. This configuration is known as tiltwing.

Most studies related to tiltrotors have been carried out in the United States, so several research and development projects have been launched in Europe to provide more insight in tiltrotor flows. DART [5] (Development of an Advanced Rotor for Tiltrotor) aimed to improve rotor hub designs; TILTAERO [6, 7] (Tiltrotor Interactional Aerodynamics) to study the interactional aerodynamics; and ADYN [8] (Advanced European Tiltrotor Dynamics and Noise) to investigate rotor dynamics, performance, and level of noise on tiltrotors. All these projects have provided a noticeable contribution to the tiltrotor knowledge base.

Unlike conventional tiltrotor configurations, tiltwing aircraft have not been widely studied. To fill this gap, the research project NICETRIP [9] (Novel Innovative Competitive Effective Tilt Rotor Integrated Project) was funded by the European Union (EU) to develop a database covering aerodynamic interactional phenomena and other technological aspects of tiltwing vehicles. In this framework, a 1:5 motorised model-scale tiltrotor was designed and manufactured under the name of ERICA (Enhanced Rotorcraft Innovative Concept Achievement) [10] and experiments were undertaken using the 9.5×9.5m DNW-LLF (German-Dutch Wind Tunnels Large Low-speed Facility) and the 8m S1MA ONERA wind tunnels. The tests covered the full flight envelope from helicopter mode, where the nacelles were tilted 90 degrees relative to the aircraft axis, to aeroplane mode, for a range of angles of attack (AoA) and freestream Mach numbers (M_∞). Helicopter and transition conversion configurations were studied at low speed (M_∞ 0 to 0.168) in the DNW-LLF

wind tunnel [11] due to its larger test section, minimising wake reingestion in the test chamber. By contrast, the high speed tests (M_∞ 0.168 to 0.55) were conducted in the test section no.2 (45m^2) of the S1MA ONERA wind tunnel [12].

Concerning numerical simulations of tiltrotors, only a few complete studies are found in the literature. Gates [13] performed numerical simulations on the isolated full-scale XV-15 rotor blades in helicopter and aeroplane modes using the HMB CFD solver, where good agreement was found with the experimental data [14–16] for both configurations. In the framework of the TILTAERO and ADYN projects, Decours *et al.* [8] carried out aerodynamic and aeroacoustic optimisations of the TILTAERO tiltrotor blade. The optimal blade was referred to as ADYN blade, and the level of noise was decreased by 4dB in take-off mode and by 6dB in landing mode [17]. Further studies have also been published for the V-22 tiltrotor using numerical simulations. The drag polar of the V-22 aircraft has been measured in the 20×20ft Boeing V/STOL wind tunnel (BVWT) [18] and the results were compared against CFD predictions from the FUN3D and OVERFLOW CFD codes [19]. Neither CFD nor experiments considered the effect of the rotors. The experiments considered a model of the V-22 of 0.15 scale and provided integrated lift, drag, and moment data. In general, the authors state that good agreement between the CFD and experiments was obtained but further studies were recommended to ensure mesh independent results can be obtained.

In 2014, an experimental validation of the 1:5 model-scale ERICA tiltrotor was carried out by Decours *et al.* [20], using the state-of-the-art helicopter aerodynamic CFD solvers in Europe. Two flight configurations, corresponding to minimum speed and highly loaded aeroplane and transition corridor modes, were simulated using different CFD tools, methodologies, turbulence models, and grids with the aim to characterise the aerodynamic interactional phenomena on the ERICA tiltrotor. Concerning the aeroplane mode configuration, experiments predicted a local separation at the top of the fuselage near the centre-line and the fixed wing junction. Not all CFD solvers were able to well reproduce the flow separation on the fuselage, though a fair agreement has been obtained between CFD and experiments, overall.

In this work, we perform numerical simulations of the ERICA tiltrotor using high-fidelity computational fluid dynamics. The aim of this work is to assess the capability of the present CFD method in accurately predicting tiltrotor loads at different flight configurations. In this regard, three representative flight configurations of the ERICA were selected, corresponding to aeroplane, transition corridor, and helicopter modes, covering all modes of tiltrotor flight. The rotor blades were fully resolved and the use of a uniform and non-uniform actuator disk was put forward to quantify the effect of the rotor on the fuselage loads. A fundamental investigation of the effect of the aerodynamic interference between rotor and wings on the tiltwing aircraft is also shown, and this has not been reported elsewhere in the literature. The comparison of results with fully resolved blades and actuator disks is also novel.

The structure of this paper is as follows: Section II describes the CFD solver used and the methodology employed to represent the rotor blades. Section III presents the mesh generation and multi-block topology employed for each individual component. Section IV summarises the test cases selected for computations, and section V presents the numerical results. At first, the aeroplane configuration results are shown, to assess

5

the effect of different methods in modelling the rotor blades on the airloads of the ERICA. Then, transition corridor and helicopter configuration results are presented. Finally, conclusions and future work are given in Section VI.

II.   HMB Solver

The Helicopter Multi-Block (HMB) [21] code is used as the CFD solver for the present work. It solves the Unsteady Reynolds Averaged Navier-Stokes (URANS) equations in integral form using the arbitrary Lagrangian-Eulerian (ALE) formulation, first proposed by Hirt *et al.* [22], for the time-dependent domains, which may include moving boundaries. The Navier-Stokes equations are discretised using a cell-centred finite volume approach on a multi-block grid. The spatial discretisation of these equations leads to a set of ordinary differential equations in time,

$$\frac{d}{dt}(\boldsymbol{W}V) = -\boldsymbol{R}(\boldsymbol{W}),\tag{1}$$

where $\boldsymbol{W}$ and $\boldsymbol{R}$ are the flow solution and flux residual vectors, respectively, and V is the volume of the cell. To evaluate the convective fluxes, Osher [23] and Roe [24] approximate Riemann solvers are used in HMB, while the viscous terms are discretised using a second order central differencing spatial discretisation. The Monotone Upstream-centred Schemes for Conservation Laws (MUSCL) developed by van Leer [25] is used to provide third order accuracy in space. The HMB solver uses the alternative form of the Albada limiter [26] being activated in regions where a large gradients are encountered, mainly due to shock waves, avoiding the non-physical spurious oscillations. An implicit, dual-time stepping method is employed to perform the temporal integration. The solution is marching in the pseudo-time to achieve fast convergence, using a first-order backward difference. The linearised system of the Navier-Stokes equations is solved using the Generalised Conjugate Gradient (GCG) method with a Block Incomplete Lower-Upper (BILU) factorisation as a pre-conditioner [27]. Because implicit scheme requires small Courant-Friedrichs-Lewy (CFL) at the early iterations, some explicit iteration using the forward Euler method or the four stage Runge-Kutta method (RK4) by Jameson [28] should be computed to smooth out the initial flow. Multi-block structured meshes are used for HMB, which allow easy sharing of the calculation load in parallel computing.

An overset grid and sliding plane methods are available in HMB [29, 30] to allow the relative motion between different components. Both methods have been widely employed for isolated rotor blades, such as the UH-60A by Dehaeze *et al.* [31], S-76 by Jimenez and Barakos [32], XV-15 tiltrotor blades by Gates [13], and complete helicopter configurations [29]. For the present work, an overset grid method is employed to explore its capabilities with tiltrotor configurations.

A.   Aerodynamic Models

Two aerodynamic methods are employed to model the rotor blades. The higher fidelity method includes the geometry of the blades in the computational domain and it will be referred to as fully resolved blade (FRB). This methodology provides a full representation of the wake and detailed information of the source of unsteadiness of the flow. Furthermore, the boundary layers on the blades are resolved so the method

6

provides the best estimate loads. The other aerodynamic models presents here are the actuator disks (AD) [33], which simulate the effect of the rotor blades by creating a pressure jump across an infinitesimally thin disk. These methods are useful in predicting loads on the fuselages.

The two actuator disk models employed here are described below. The first model is a uniform rotor actuator disk (URAD) in loading while the second model allows for a variable disk loading as function of the rotor radius (NURAD, Non-Uniform Rotor Actuator Disk).

As previously introduced, the actuator disk simulates the effect of the rotor blades by creating a pressure difference on a single plane. For the case of uniform rotor actuator disk, the pressure jump in non-dimensional form is:

$$\Delta P^* = \frac{T}{\rho_\infty V_\infty^2 \mathcal{S}_{\text{rot}}}, \tag{2}$$

where the thrust coefficient is defined as $C_T = \dfrac{T}{\rho_\infty V_{\text{tip}}^2 \mathcal{S}_{\text{rot}}}$ with $\mathcal{S}_{\text{rot}}$ being the rotor disk area.

The non-uniform rotor actuator disk calculates the jump of pressure across the disk plane based on Shaidakov's method [34]. This approach results in a non-uniform pressure distribution and as a function of radial position along the blade (r) and blade azimuth Ψ. The model is based on the following equation:

$$\Delta P^* = P_0 + P_{1S} \sin(\Psi) + P_{2C} \cos(2\Psi), \tag{3}$$

where the coefficients P_0, P_{1S} and P_{2C} depend on rotor radius and solidity, rotor attitude, advance ratio, thrust coefficient, lift coefficient slope, and freestream velocity. The model is detailed in [34, 35].

Figure 1 shows an overview of the relative position of the actuator disk for the ERICA tiltrotor for the transition corridor (left) and for the helicopter mode configurations (right).

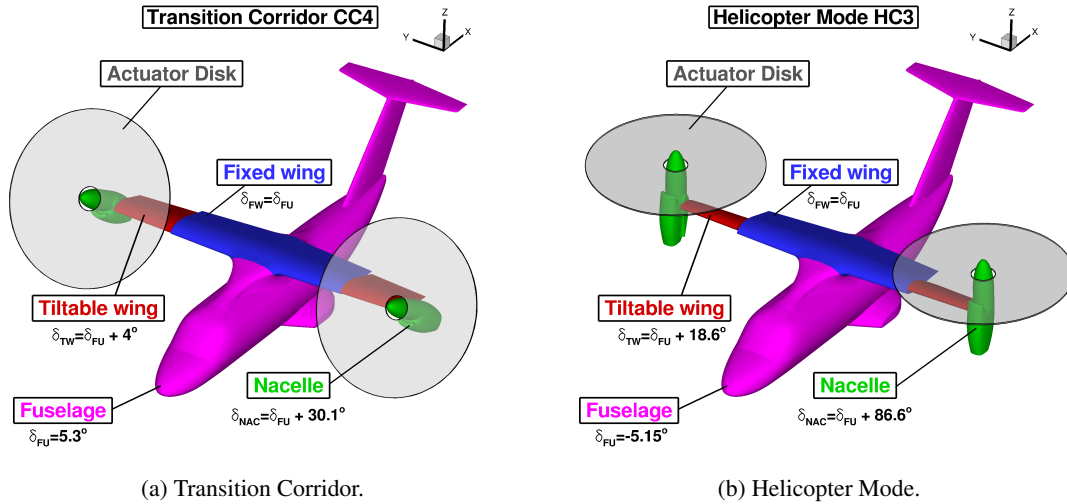(a) Transition Corridor.

(b) Helicopter Mode.

Fig. 1: Set-up of the transition corridor CC (left) and helicopter mode HC (right) configurations with the rotor actuator disk.

III.   Mesh Generation

The chimera method was employed to ease the generation of the different structured multi-block grids. For all configurations, self-contained component grids for the main fuselage and the nacelle-tiltable wing were built, while four ADYN blades were embedded in the nacelle mesh component. To enable the relative motion between nacelle and tiltable wing so as tiltable and fixed wing, an independently generated overlapping grid sets were used, employing a 4mm gap. Likewise, a gap between the blade root and spinner for the full blade representation was allowed. A Cartesian off-body mesh was used as the background to capture the convection of the tip vortex generated by the blades. Table 1 compares the mesh size used here for CFD computation. If the actuator disk methodology is used, a reduction of the mesh size of about 20% and 18% for the aeroplane and transition corridor/helicopter modes is achieved.

Table 1: ERICA model-scale component mesh sizes, given as million nodes.

Components	Aeroplane Mode	Transition Corridor	Helicopter Mode
Fuselage and fixed wing	9.9	9.9	9.9
Tiltable wing	-	3.6	3.6
Nacelle	30.3	10.9	10.9
Rotor blades (x4)	11.4	11.4	11.4
Wind tunnel	4.6	27.6	27.6
Total	**56.2**	**63.4**	**63.4**

Figure 2 shows a detailed view of the surface mesh and the multi-block topology of the ERICA's nacelle. To match the wind tunnel model [11, 12], the engine inlet was treated as solid. In the longitudinal direction of the nacelle, 270 mesh points are used, while 422 points are used around the nacelle. In the wall normal direction (see Figure 2b) 41 points are used. That mesh spacing corresponds to a y-plus of about 0.15. A C-topology around the leading edge of the connection with the tiltable wing was chosen, whilst an O-topology was used at the nose and rear part of the nacelle.

Figure 3 shows a view of the surface and body-fitted mesh around the fuselage. An O multi-block topology was built at the front and rear parts of the fuselage, whereas a C-H multi-block topology was generated around the wing and horizontal stabiliser (see Figure 3b). In the chordwise direction around the fixed wind, 310 points are used, with 138 around the horizontal stabiliser. The distribution of points normal to the fixed wing and fuselage, follow and exponential law with the first point located at $4 \cdot 10^{-6}$ of the reference length (L_{ref}), leading to a y-plus of about 0.15.

The multi-block overset arrangement of the ERICA tiltrotor for the case of the aeroplane mode is shown in Figure 4. Farfield and symmetry boundary conditions were applied at the background level, while chimera boundaries were used at the nacelle, blades, and fuselage components. The wind tunnel model support was not modelled.
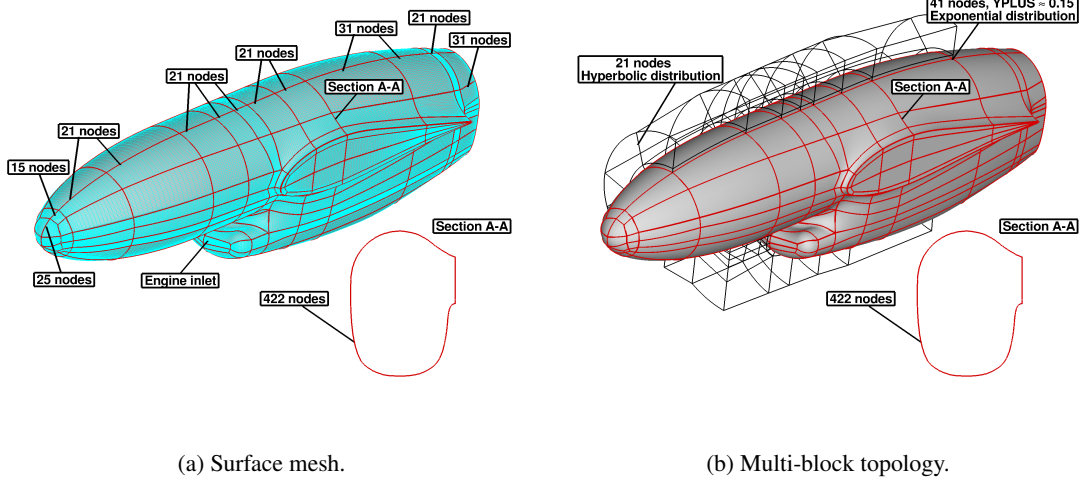
(a) Surface mesh.   (b) Multi-block topology.

Fig. 2: ERICA's nacelle structured mesh domain, topology, and surface mesh detail.

(a) Surface mesh.   (b) Multi-block topology.

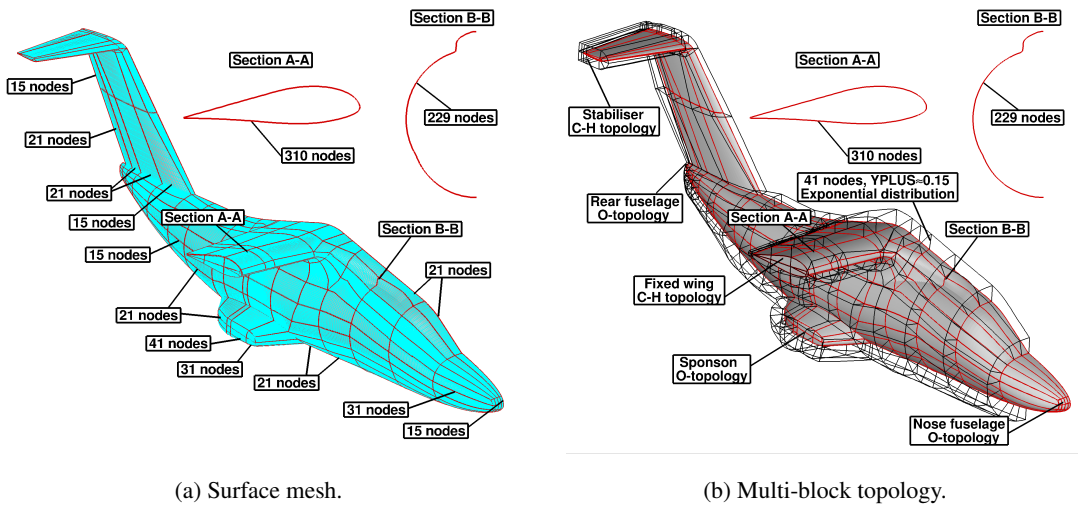Fig. 3: ERICA's fuselage structured mesh domain, topology, and surface mesh detail.

IV. Numerical and Test Condition Details

Table 2 summarises the conditions for each test case computed. The first configuration is labelled as AC1 (aeroplane configuration), and refers to a very low speed aeroplane-mode M_∞ = 0.168, along with a large aircraft AoA of δ_{FU} = 10.02 degrees. Neither the nacelles nor the tiltable wings were tilted with respect to the fuselage ($\delta_{FU} = \delta_{NAC} = \delta_{TW}$). The second case corresponds to a typical tiltrotor transition corridor configuration with a moderate angle of attack of 5.30 degrees, labelled as CC4. Unlike the AC1, the nacelle was significant rotated respect to the fuselage ($\delta_{NAC} = \delta_{FU}$+30.1), while a small rotation of the tiltable wing ($\delta_{TW} = \delta_{FU}$+4.0) was allowed. Finally, a helicopter configuration labelled as HC3 was also selected for computation. This configuration HC3 is characterised for a moderate forward speed (M_∞ = 0.104) with an aircraft angle of attack of -5.15 degrees and the nacelles tilted 86.6 degrees respect to the fuselage. The Reynolds numbers,

9

(a) Multi-block grid.

(b) Cross section of the multi-block grid.
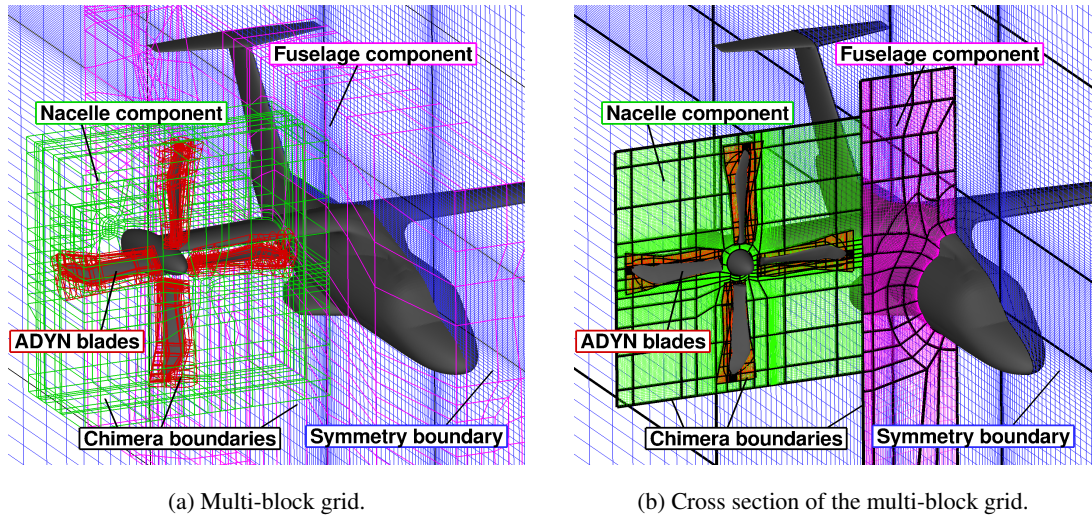
Fig. 4: Details of the multi-block overset arrangement of the ERICA tiltrotor in aeroplane mode configuration. Blue line=background component; Purple line=fuselage component; Green line= nacelle component; Grey line=blade component.

based on the reference length L_{ref} and on the freestream velocity V_∞, were $1.70 \cdot 10^6$ and $1.16 \cdot 10^6$ for the AC1/CC4 and HC3 cases respectively. Figure 5 shows the different test conditions employed here, and the nacelle pitch angle as function of the freestream Mach number.

Table 2: Test conditions for the selected cases [36, 37]. AC1=Aeroplane Mode; CC4=Transition Corridor; HC3=Helicopter Mode.

Parameters	Aeroplane Mode AC1	Transition Corridor CC4	Helicopter Mode HC3
M_∞	0.168	0.168	0.104
M_{tip}	0.470	0.603	0.560
$\mu = M_\infty/M_{tip}$	0.357	0.278	0.185
Re_{ref}	$1.70 \cdot 10^6$	$1.70 \cdot 10^6$	$1.16 \cdot 10^6$
δ_{FU} [deg]	$10.02°$	$5.30°$	$-5.15°$
δ_{NAC} [deg]	$10.02°$	$35.40°$	$81.45°$
δ_{TW} [deg]	$10.02°$	$9.30°$	$13.45°$
RPM blade rotor	2130	2730	2490
$\theta_{75\%}$ [deg]	$27.36°$	$16.6°$	$9.0°$

Table 3 summarises the cases performed for the ERICA tiltrotor. Considering the aeroplane configuration AC1, several cases were computed. The rotor blades were represented by means of a uniform rotor actuator disk (case #1), non-uniform rotor actuator disk (case #2), and fully resolved blade (case #3). To quantify the effect of the aerodynamic interference between the rotor and wing of the ERICA, case #4 was simulated which did not include any rotor. For all these cases, a half model of the aircraft was included in the computational domain, employing symmetry boundary conditions. The complete aircraft was simulated

10
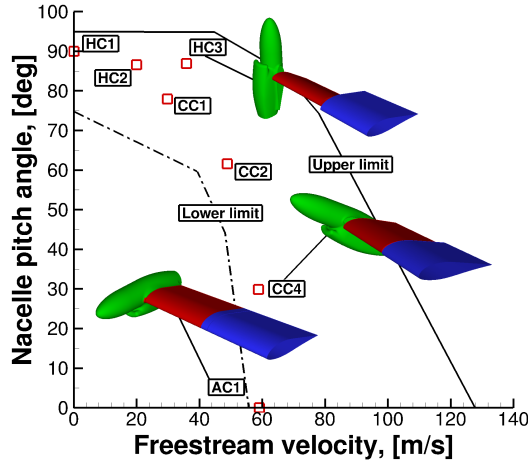
Fig. 5: Trimmed test conditions for the ERICA tiltrotor reported by Bruin *et al.* [36]. AC1 (Aeroplane configuration), CC4 (Transition Corridor), and HC3 (Helicopter configuration) were selected for numerical computations.

using a uniform rotor actuator disk (case #6), with the aim to investigate the effect of the symmetry boundary conditions on the top fuselage centre-line. The transition corridor configuration was also computed using a uniform rotor actuator disk (case #6) and fully resolved blades (case #7). The helicopter case HC3 was computed using a steady-state flow approach with the rotor blades modelled via a uniform actuator disk (case #8). Unsteady Reynolds Averaged Navier-Stokes computations were used for the cases with fully resolved blades, and steady RANS was used for cases with actuator disk models.

All the flow solutions were computed by solving the RANS/URANS equations, coupled with Wilcox's k-ω turbulence model [38]. This was based only on experience and the reputation of this model for stability. The flow equations were integrated with the implicit dual-time stepping method of HMB, using a pseudo-time CFL equal to 4 for the RANS cases. For the URANS cases, the selected time step corresponded to half a degree of rotor revolution.

Table 3: Computational cases for the 1:5 model-scale ERICA tiltrotor. St=Steady; Uns=Unsteady; URAD=Uniform Rotor Actuator Disk; NURAD=Non-Uniform Rotor Actuator Disk; FRB=Fully Resolved Blade; Free=Neither Rotor Actuator Disk nor Propeller; S-S=Semi-Span; F-S=Full-Span.

ID Case	Configuration	St/Uns	Methodology	Semi/Full Span
#1	AC1	Steady	URAD	S-S
#2	AC1	Steady	NURAD	S-S
#3	AC1	Unsteady	FRB	S-S
#4	AC1	Steady	Free	S-S
#5	AC1	Steady	URAD	F-S
#6	CC4	Steady	URAD	S-S
#7	CC4	Unsteady	FRB	S-S
#8	HC3	Steady	URAD	S-S

V.   Results and Discussion

To assess the capability of the present CFD method in accurately predicting tiltrotor flows, twenty one cross-sections were selected for C_P profile comparisons between CFD and experiments [11, 12] (see Table 4). Two sections were selected on the top and bottom symmetry planes of the fuselage (labelled with SYM-TOP and SYM-BOT respectively), four sections on the fixed wing (labelled with FW), three on the tiltable wing (labelled with TW) which define the zone of aerodynamic interaction between the tiltable wing and the blades, four on the nacelle (labelled with NA), and eight on the fuselage (labelled with FU). Figure 6 shows the position of the selected sections on the ERICA tiltrotor for the aeroplane mode AC1.

Considering the AC1 configuration, C_P was analysed for the FRB, URAD, and NURAD approaches. The first goal was to evaluate the ability of the aerodynamic methods in producing adequate estimates of the loads at the aerodynamic interaction zone. The second goal was to investigate if results of the AD provide good agreement of the loads on the fuselage. Total loads on the ERICA tiltrotor and visualisation of the flowfield using iso-surfaces of the $\bar{Q}$-criterion are also presented for the FRB approach. Finally, results for the transition corridor and helicopter mode configurations will be compared through C_P distribution on the selected stations with the experimental data.

Table 4: Nomenclature of the stations selected for C_P profile comparisons. BOT=Bottom; FU=Fuselage; FW=Fixed Wing; NA=Nacelle; TW=Tiltable Wing; SYM=Symmetry.

Nomenclature	Description
SYM-TOP	Fuselage symmetry plane (top), station y=0 mm.
SYM-BOT	Fuselage symmetry plane (bottom), station y=0 mm.
FW-A	Fixed wing, station y=280 mm.
FW-B	Fixed wing, station y=490 mm.
FW-C	Fixed wing, station y=700 mm.
FW-D	Fixed wing, station y=805 mm.
TW-A	Tiltable wing, station y=855 mm.
TW-B	Tiltable wing, station y=955 mm.
TW-C	Tiltable wing, station y=1117.5 mm.
NA-A	Nacelle (top), y=1500 mm.
NA-B	Nacelle (bottom), y=1500 mm.
NA-C	Nacelle (central), x=1560 mm.
NA-D	Nacelle (rear), x=1860 mm.
FU-A	Fuselage, station x=260 mm.
FU-B	Fuselage, station x=535 mm.
FU-C	Fuselage, station x=810 mm.
FU-D	Fuselage, station x=1163 mm.
FU-E	Fuselage, station x=1470 mm.
FU-F	Fuselage, station x=1810 mm.
FU-G	Fuselage, station x=2460 mm.
FU-H	Fuselage, station x=2760 mm.

(a) Sections on the fixed and tiltable wings.   (b) Sections on the fuselage.
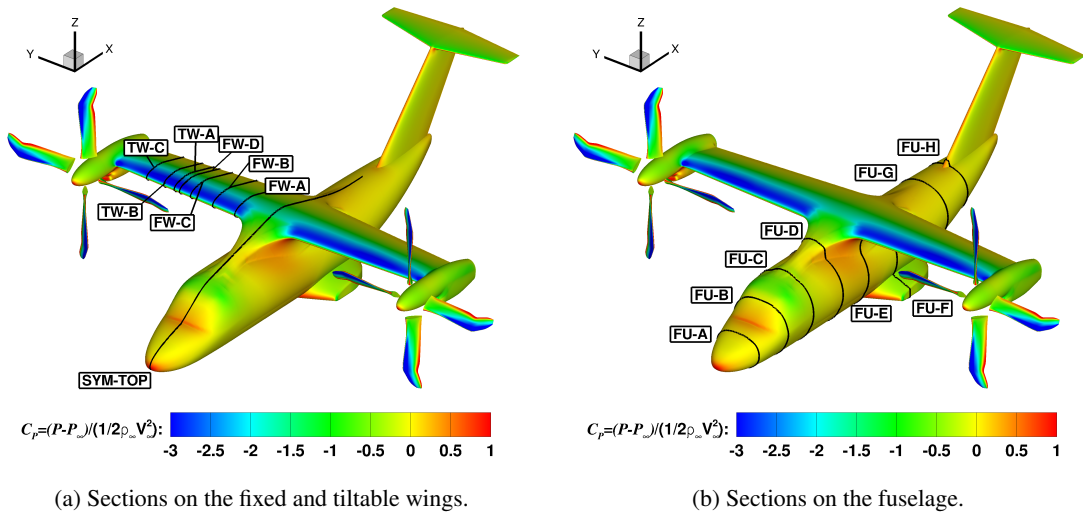
Fig. 6: Cross-sections selected for comparisons between CFD and experiments [11, 12] on the fixed and tiltable wings, and fuselage of the ERICA tiltrotor for the aeroplane mode configuration.

A. Aeroplane Mode AC1

1. C_P profile comparisons

C_P profile comparisons between CFD and experiments [11, 12] on the fuselage, fixed and tiltable wings of the ERICA tiltrotor are given in Figure 7. They correspond to the top fuselage centre-line and inner, middle, and outer tiltable and fixed wing sections. The CFD results were not averaged in phase, which could lead to a source of error in the comparison. For the FRB cases, C_P values were averaged over the last computed rotor revolution instead of time-averaging. Regarding the C_P profile at the centre-line of the fuselage (Figure 7a), a zone of recirculation is seen by both sets of experiments (Modane and DNW experiments are denoted by squares and triangles, respectively) represented by a pressure plateau after the wing leading edge suction peak. The HMB predictions (URAD=green line, NURAD=blue line, FRB=red line) overestimate the suction peak ($C_{P \text{ URAD}}$= 1.70; $C_{P \text{ NURAD}}$= 1.70; $C_{P \text{ FRB}}$= 1.66; $C_{P \text{ DNW}}$= 1.25; $C_{P \text{ ONERA}}$= 1.18) and do not capture the region of recirculation. This can be due to a failure of the employed turbulence model, wind tunnel effects, and lack of exact trimmed conditions. By contrast, the CFD results at the front and rear part of the fuselage are in close agreement with the experimental data. Considering the inner fixed wing section (Figure 7b), experiments suggest that this region is separated due to the presence of a plateau on the C_P data. CFD predictions slightly overestimate the suction peak and the pressure plateau is not well reproduced. This is consistent with the flowfield predicted in Figure 7a.

In the middle and outer fixed wing sections (Figures 7c-7e), wind tunnel experiments show a good agreement, with small differences of 9% for the suction peak. Results show good agreement with the experiment at all stations, even if the trailing edge pressure plateau is slightly under-estimated. Regarding the zone of aerodynamic interaction located near the tiltable wing sections (Figures 7f-7h), good agreement between CFD and experimental results is observed. Moreover, results of the CFD with the actuator disk produced adequate

13

estimates of the C_P profile with a small discrepancy of 1.59% on the suction peak between both approaches. As can be seen, negligible differences were found between the URAD and NURAD results for all stations. Note that the differences between the two sets of experiments are always larger than the differences between FRB and AD results.

Using the URAD loads as a reference, the effects of using half or complete aircraft geometries with or without rotor modes can be assessed in terms of pressure distributions, in Figure 8. For all stations, numerical simulations for the whole aircraft (referred to as URAD F-S) have a negligible impact on the C_P if compared with predictions using symmetry (referred to as URAD). Regarding the effect of prop rotor on and off (referred to as Free) on the loads, it can be observed that the centre-line of the fuselage and the fixed-wing regions are weakly influenced by the wake-body interaction. The tiltable wing regions, however, are strongly affected by the interactional process, thus giving rise to a larger increase in the normal (C_n) and tangential (C_t) coefficients (see Figures 8g-8h).

Figure 9 shows C_P profile comparisons on the nacelle component, corresponding to the top and bottom centre lines, and the central and rear sections of the nacelle (see Figure 9c). Considering the top and bottom centre-line sections (Figures 9a-9b), a noticeable scatter of C_P is observed for both sets of experiments. The CFD results were able to capture the averaged trend of the experimental C_P for both sections, where the results with the actuator disk provided slightly higher C_P values compared to the fully resolved blades. Finally, for the middle and rear part of the nacelle (Figures 9d-9e), good agreement is shown between CFD and experiments.

Figure 10 presents C_P comparisons on the ERICA fuselage at eight cross-sections. As can been seen, all CFD curves are close to the experimental data. Better agreement is obtained at the front of the fuselage (see Figures 10a-10d), where the flowfield is attached. The HMB solution appears to capture well all features shown by the experiments. Even for stations located behind the fixed wing (see Figures 10e-10h), the agreement is still fair near the spoonsons and the fin of the model. It is noticeable that discrepancies appear not to be present when the actuator disk approaches were employed, which encourages the use of this approach in predicting loads on the fuselage.

The effect of the model support on the ERICA tiltrotor results was also assessed using the average C_P distribution on the bottom part of the fuselage in Figure 11. The model of the DNW-LLF was supported via a ventral sting set-up at the rear part of the fuselage, whilst a straight sting was set-up in the ONERA model. As can be seen in Figure 11, the model support on the fuselage is stronger for the DNW-LLF, and less intrusive for the ONERA model. From a numerical point of view, HMB predictions compare well with the experimental data of ONERA, where the support is straight. This is consistent with the fact that the model support was not modelled in the computational domain. Furthermore, no discrepancies were found between FRB and AD results, which may suggest that this zone is not influenced by details of the rotor blades.

In this section, the integrated loads generated on the nacelle, tiltable wing, and the rest of the fuselage with the fixed wing are analysed for the aeroplane configuration with the fully resolved blade approach. Lift and drag coefficients on the tiltable wing as function of the main rotor azimuth Ψ are shown in Figure 12a. The drag (C_D) and lift (C_L) coefficients are represented by squares and triangles, respectively, while their averaged values are represented with solid lines. As can be seen, the 4/rev. blade passage effect on the tiltable wing is well captured, with fluctuation values of 5.14% and 23.8% for the lift and drag, respectively. Previous work [20], reported fluctuations of lift and drag between 5%-7% and 20%-30% depending on the partner.

Likewise, the history of the loads on the nacelle is given in Figure 12b, which reveals the 4/rev. blade passage effect for both aerodynamic coefficients. The lift and drag fluctuations are 6.86% and 2.5%, respectively, which suggests that the nacelle has a milder unsteady behaviour than the tiltable wing. The fuselage and fixed wing lift and drag coefficients are presented in Figure 12c, which also reveals a 4/rev. signal behaviour due to the blade passage. The results show small fluctuations of drag (5.64%) and lift (2.17%) coefficients.

Finally, the lift and drag coefficients of the complete ERICA tiltrotor are compared with the experimental data. Table 5 shows a breakdown of the total averaged lift and drag coefficient for each component. A discrepancy of 15.51% and 33.9% for the lift and drag coefficients is found. Results reported in Decours *et al.* [20] also found a discrepancy on lift about 15%, and no drag values were reported. The NICETRIP experimental data is relatively new and not well explored by researchers. It is therefore likely that corrections must be applied to the experimental data.

Table 5: Averaged lift and drag coefficient comparisons between CFD and experiments [11, 12] for the ERICA tiltrotor.

Component	HMB3		Wind tunnel	
	C_L	C_D	C_L	C_D
Tiltable wing	0.244	0.012	-	-
Nacelle	0.039	0.017	-	-
Fuselage	0.432	0.041	-	-
Rotor	0.073	-	-	-
Total	**0.789**	**0.071**	**0.683**	**0.053**

3. Flowfield details

Visualisation of the flowfield of the ERICA tiltrotor using the $\bar{Q}$-criterion [39] coloured by Mach number is presented in Figure 13 for the fully resolved blade and uniform rotor actuator disk approaches. The quantity

Q is defined as follows:

$$Q = \frac{1}{2}(\Omega_{ij}\Omega_{ij} - S_{ij}S_{ij}), \tag{4}$$

where Ω_{ij} and S_{ij} are the antisymmetric and symmetric part of the velocity gradient, respectively:

$$\Omega_{ij} = \frac{1}{2}\left(\frac{\partial u_i}{\partial x_j} - \frac{\partial u_j}{\partial x_i}\right), \quad S_{ij} = \frac{1}{2}\left(\frac{\partial u_i}{\partial x_j} + \frac{\partial u_j}{\partial x_i}\right). \tag{5}$$

The quantity Q has the dimensions of a velocity squared divided by a length squared, and it is therefore nondimensionalised in HMB as follows:

$$\bar{Q} = Q\left(\frac{L_{\text{ref}}}{V_{\text{ref}}}\right)^2. \tag{6}$$

Regarding the FRB approach, the wake behind the rotor disk is preserved for more than one rotor diameter downstream thanks to the refined mesh employed in this region (Figure 14). This informative plot shows the interaction of the rotor wake with the nacelle and tiltable wings. From these iso-surfaces it can be seen that the rotor wake does not directly interact with the fuselage and the fixed part of the wings. Iso-surface contours of $\bar{Q}$-criterion are shown from the CFD simulations using the uniform rotor actuator disk in Figure 13b, which reveals that a detailed wake characteristics cannot be easily identified.

B.   Transition Corridor CC4

1. C_P profile comparisons

The CC4 case corresponds to a typical tiltrotor corridor configuration with a moderate angle of attack of 5.30 degrees. The tiltable wing and nacelle angles were tilted 4 and 30.1 degrees, respectively, relative to the aircraft axis. Like for the AC1 case, profile comparisons of C_P between CFD and experiment were assessed on the fuselage, fixed and tiltable wing of the ERICA tiltrotor (see Figure 15). Considering the AC1 results, no significant differences were found between the URAD and NURAD results. This support the idea of using the simplest aerodynamic model (URAD) here to compare with the FRB approach.

Considering the pressure coefficient at the centre-line of the fuselage (Figure 16a), the experiments suggest the absence of flow separation mainly due to reduction of the angle of attack by almost 5 degrees. Results show a fair agreement with both experiments, where the suction peak is slightly over-estimated ($C_{P\ \text{URAD}}$= 1.56; $C_{P\ \text{FRB}}$= 1.53; $C_{P\ \text{DNW}}$= 1.49; $C_{P\ \text{ONERA}}$= 1.39). In the inner fixed wing (see Figure 16b), a discrepancy on the suction peak is presented by both sets of experiments (21% higher for DNW that Modane). It is interesting to note that no pressure plateau is present at the experiments, which supports the idea of absence of flow separation. From a numerical point of view, the CFD results compare well with the experimental data of DNW and, where the pressure plateau is well reproduced. The same analysis can be done for the middle and outer fixed wing (Figures 16c-16f). Furthermore, small differences are found between the FRB and URAD approaches, which a maximum discrepancy of the suction peak of 1.29%.

Figures 16g-16h show C_P comparisons within the aerodynamic interaction zone. The experiments present a different behaviour of the pressure plateau near at the trailing edge, where the DNW measurements suggest that the flow is not attached (see Figure 16h). The agreement between experiments and CFD

results are still fair and minor discrepancies appear to be present when the actuator disk approach was employed. Despite that use of the actuator disk model, CFD predictions are in close agreement with the DNW experiment, which highlights the capability of this low-fidelity approach in predicting wing loads.

Finally, a quantitative assessment of C_P profile comparisons on the ERICA fuselage is done, considering eight cross-sections (Figures 17a-17h). Despite that a minor discrepancy is found between experiments in the middle of the wing (see Figure 17h), a good agreement can be seen between the two wind tunnel measurements. Like for the AC1 case, the uniform actuator disk can cope with the loads on the fuselage, where a fair agreement has been obtained.

2. *Flowfield and aerodynamic comparison between AC1 and CC4*

The visualisation of flowfield of the ERICA tiltrotor using the $\bar{Q}$-criterion iso-surface is presented in Figure 18 for the FRB and URAD solutions. Considering the FRB approach (Figure 18a), a more complex wake is developed behind the rotor disk if compared with the AC1 wake due to the stronger wake/wing interation for the CC4 configuration.

Figure 19 shows a comparison of the aeroplane and transition corridor modes for the surface pressure distributions at stations located on the fixed and tiltable wings of the ERICA tiltrotor. The DNW experimental data was selected for both modes. The freestream Mach number was kept constant (M_{∞}= 0.168), so the changes observed on the experimental and predicted peak of C_p are mainly due to the difference in the AoA and the rotor/wing interaction. The CFD and test data agree fairly well, at all stations, and the CFD captures the same difference between AC1 and CC4 as measured in the wind tunnel. This is an encouraging result regarding the use of CFD for these very complex flow cases.
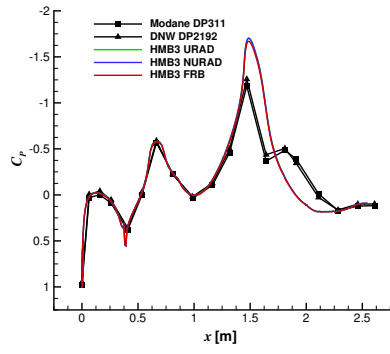
(a) SYM-TOP, section y=0 mm.
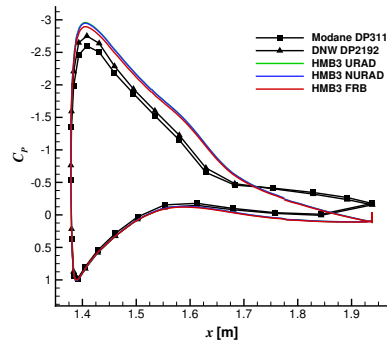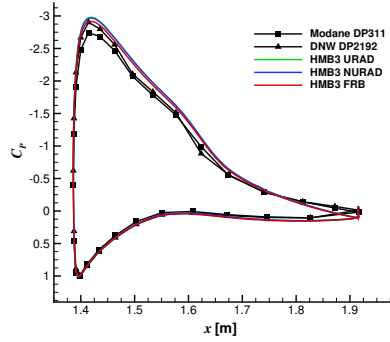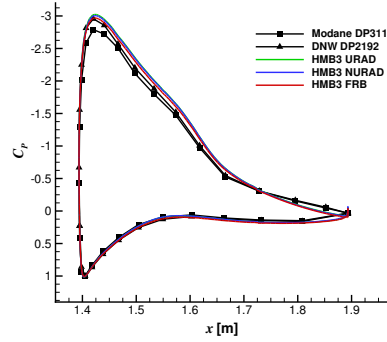
(b) FW-A, section y=280 mm.

(c) FW-B, section y=490 mm.

(d) FW-C, section y=700 mm.
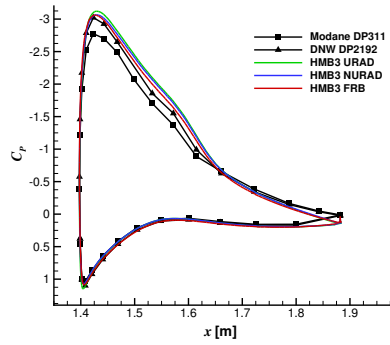
(e) FW-D, section y=805 mm.
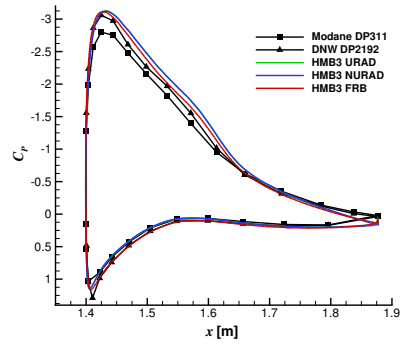
(f) TW-A, section y=855 mm.
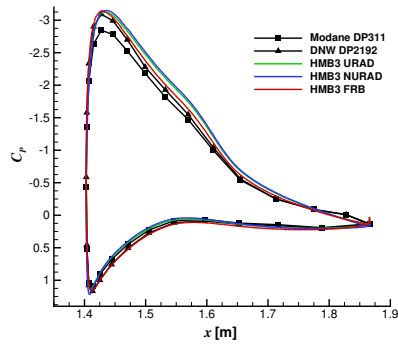
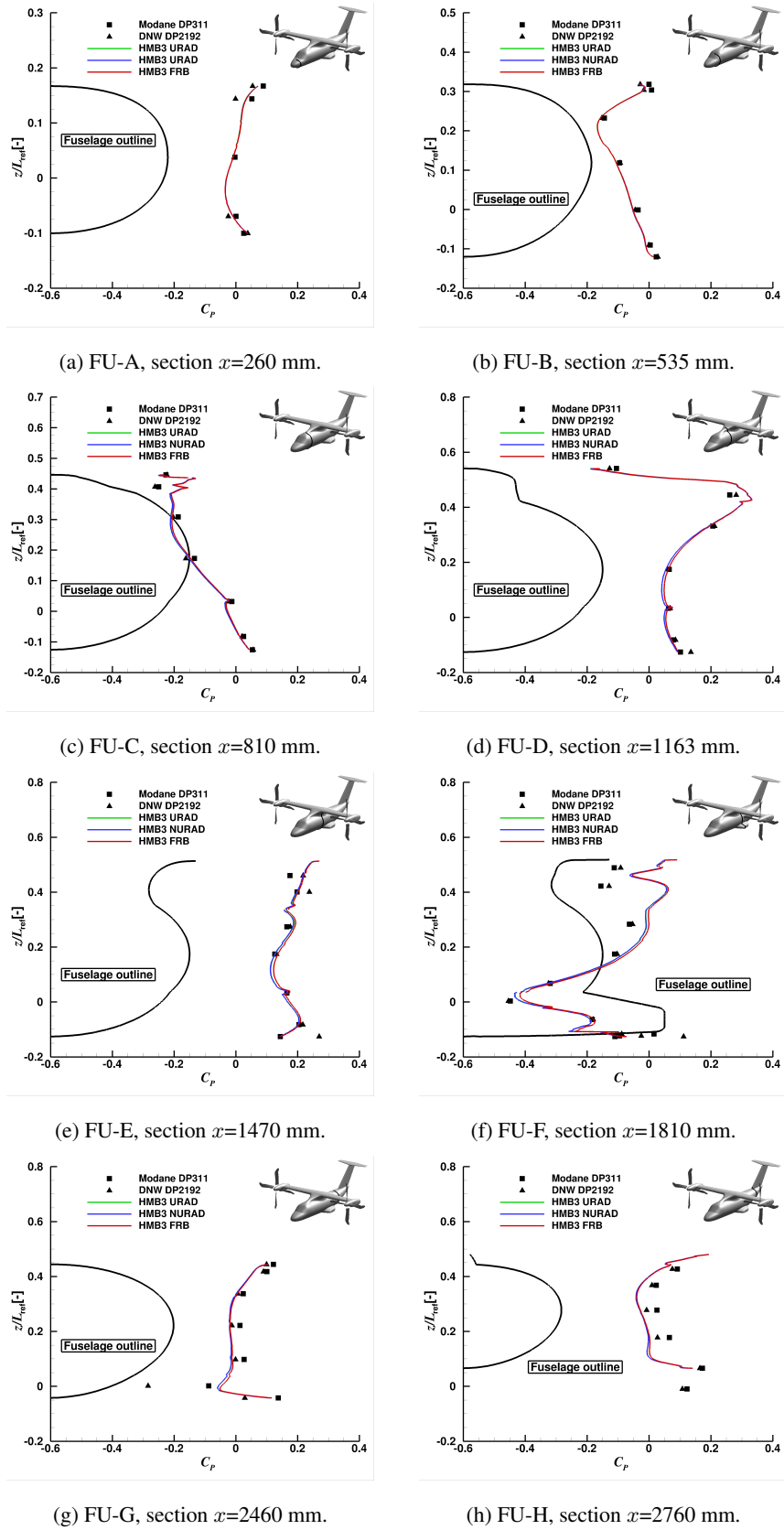(g) TW-B, section y=995 mm.
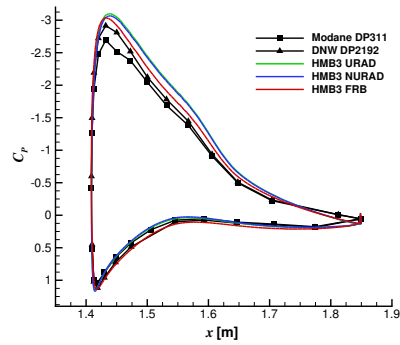
(h) TW-C, section y=1117 mm.

Fig. 7: C_P profile comparisons between CFD and experiments [11, 12] on the fixed and tiltable wings of the ERICA tiltrotor for the aeroplane mode configuration AC1.

18

(a) SYM-TOP, section y=0 mm.

(b) FW-C, section y=700 mm.

(c) FW-D, section y=805 mm.

(d) TW-A, section y=855 mm.

(e) TW-B, section y=995 mm.

(f) TW-C, section y=1117 mm.
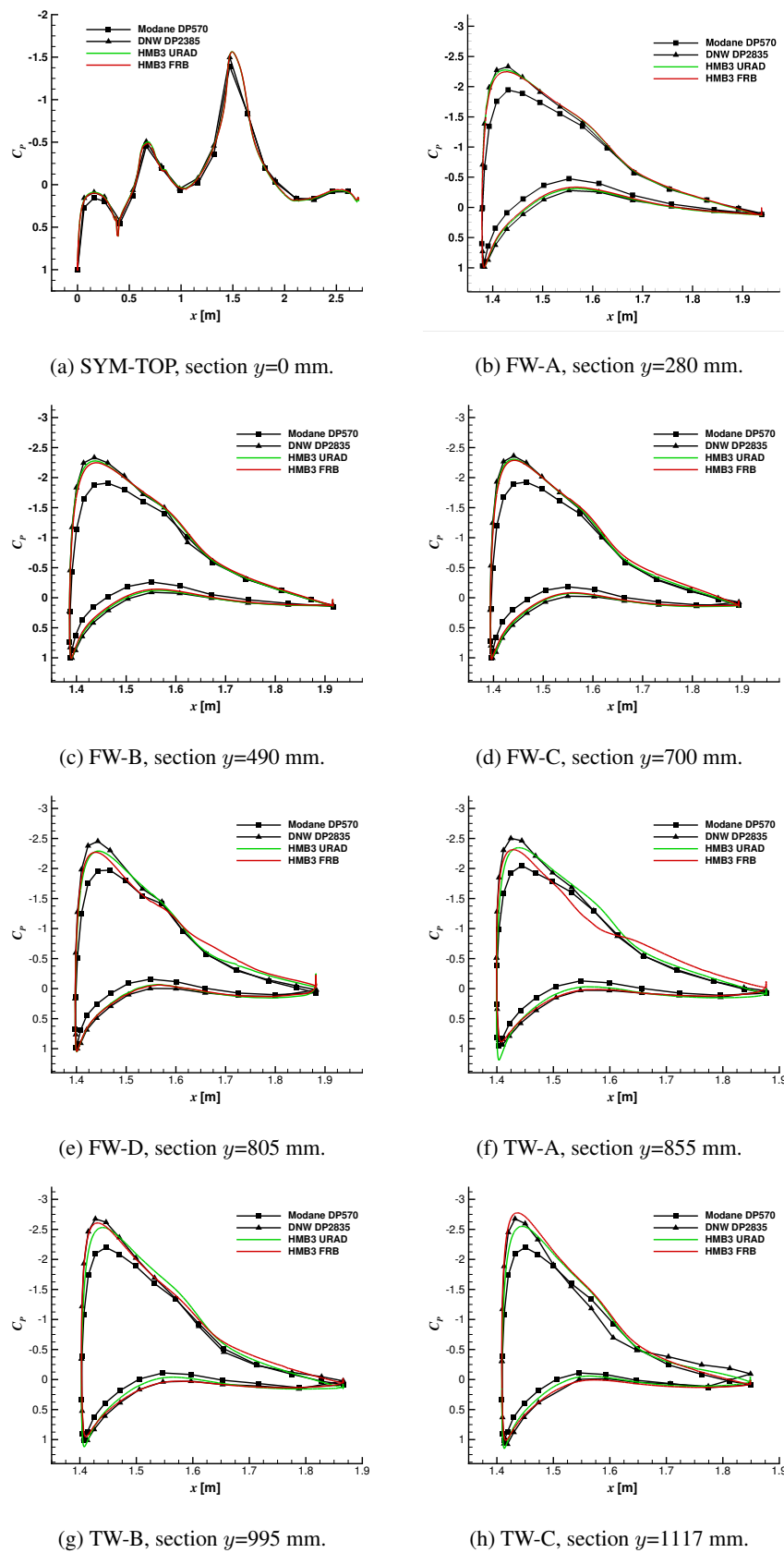
(g) Normal coefficient, C_n.

(h) Tangential coefficient, C_t.
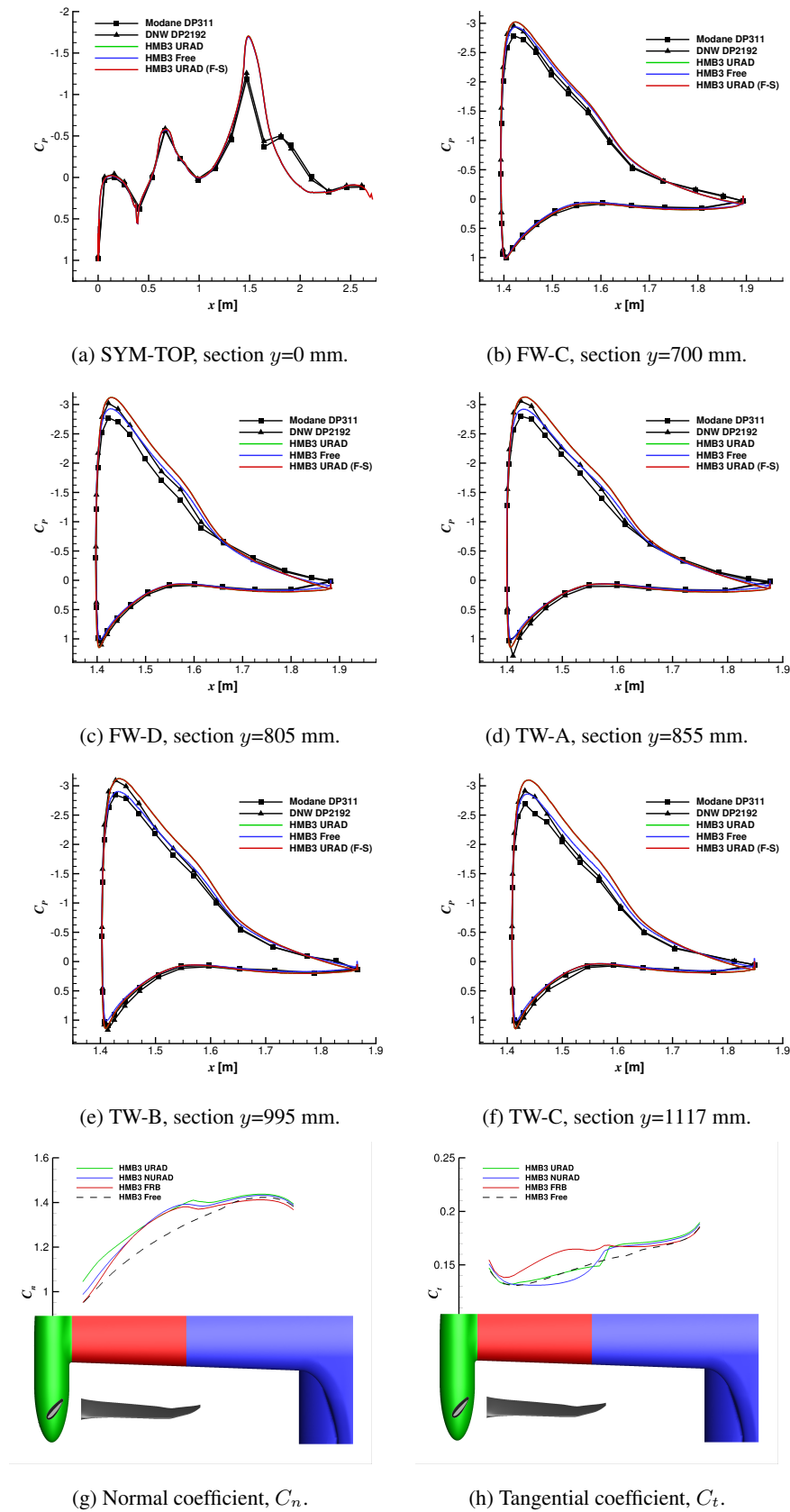
Fig. 8: C_P profile comparisons between CFD and experiments [11, 12] on the fixed and tiltable wings of the ERICA tiltrotor for the aeroplane mode configuration AC1 (a-f). Effect of the aerodynamic interference between the rotor and wing of the ERICA (g-h).

19
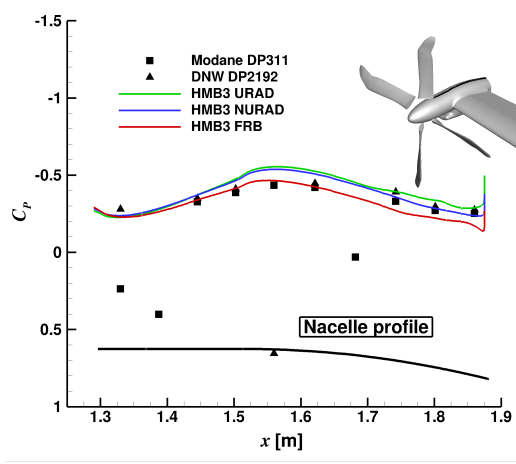
(a) NA-A, section y=1500 mm.
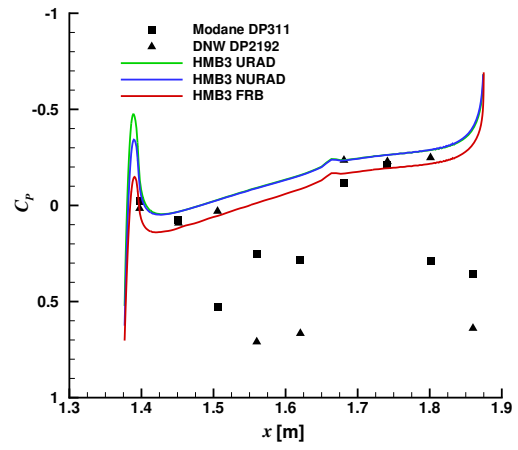
(b) NA-B, section y=1500 mm.

$C_P=(P-P_\infty)/(1/2\rho_\infty V_\infty^2)$:
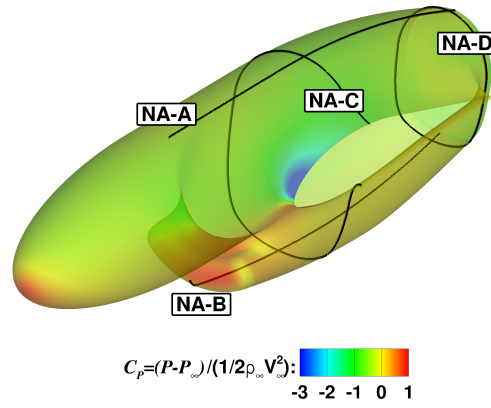
(c) Location of the cross-sections.
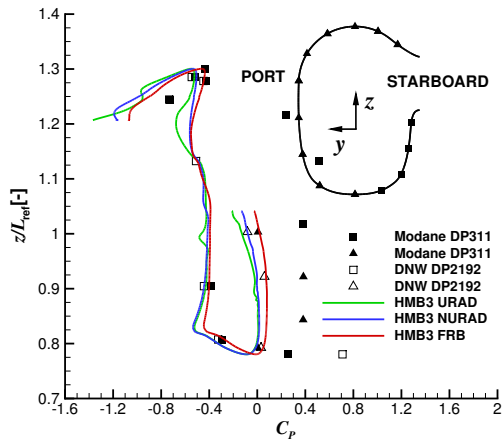
(d) NA-C, section x=1560 mm.
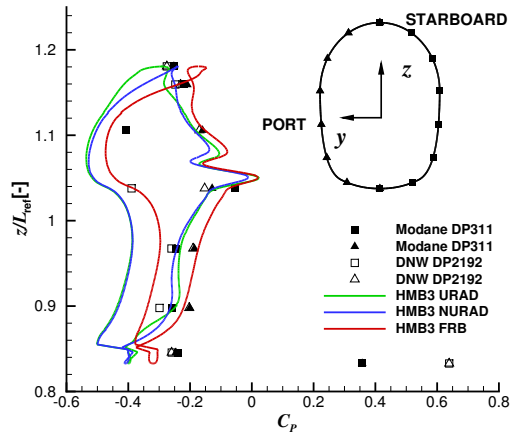
(e) NA-D, section x=1860 mm.

Fig. 9: C_P profile comparisons between CFD and experiments [11, 12] on the nacelle of the ERICA tiltrotor for the aeroplane mode configuration AC1.

(a) FU-A, section x=260 mm.

(b) FU-B, section x=535 mm.

(c) FU-C, section x=810 mm.

(d) FU-D, section x=1163 mm.

(e) FU-E, section x=1470 mm.

(f) FU-F, section x=1810 mm.

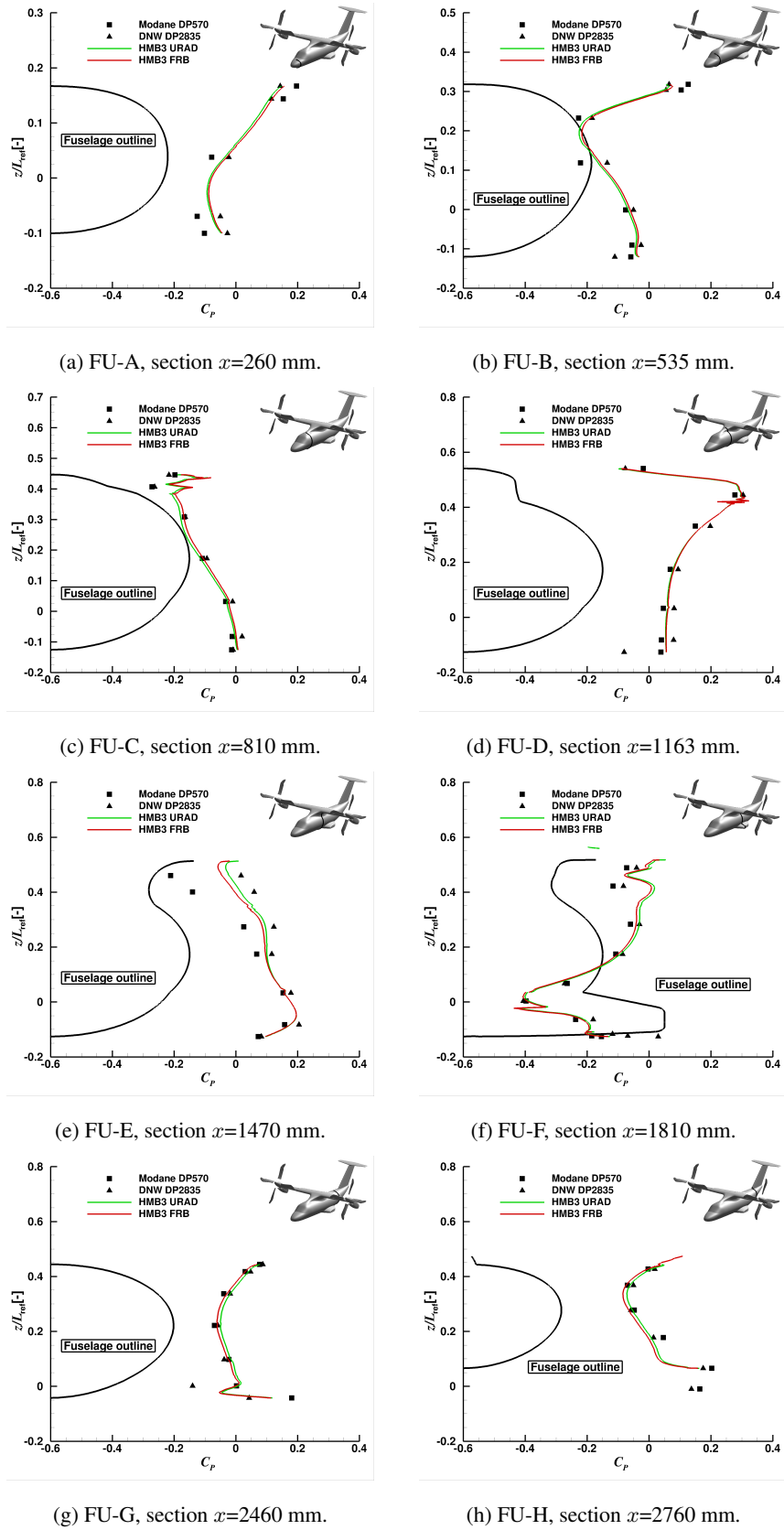(g) FU-G, section x=2460 mm.

(h) FU-H, section x=2760 mm.

Fig. 10: C_P profile comparisons between CFD and experiments [11, 12] on the fuselage of the ERICA tiltrotor for the aeroplane mode configuration AC1.
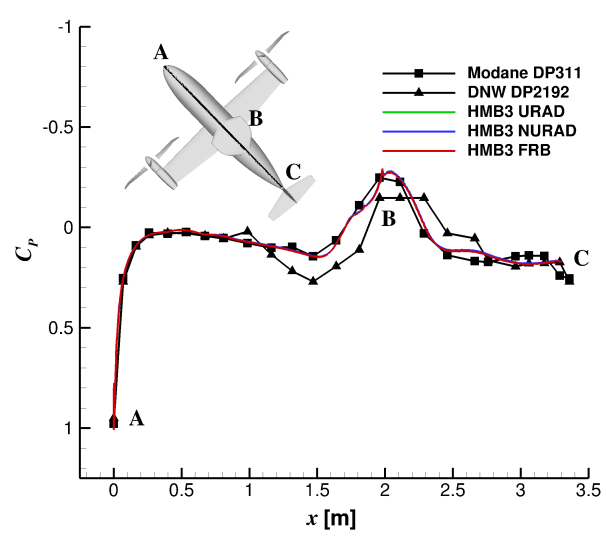
Fig. 11: C_P profile comparisons between CFD and experiments [11, 12] on the bottom part of the fuselage of the ERICA tiltrotor for the aeroplane mode configuration AC1.

(a) Loads on the tiltable wing.

(b) Loads on the nacelle.

(c) Loads on the fuselage and fixed wing.
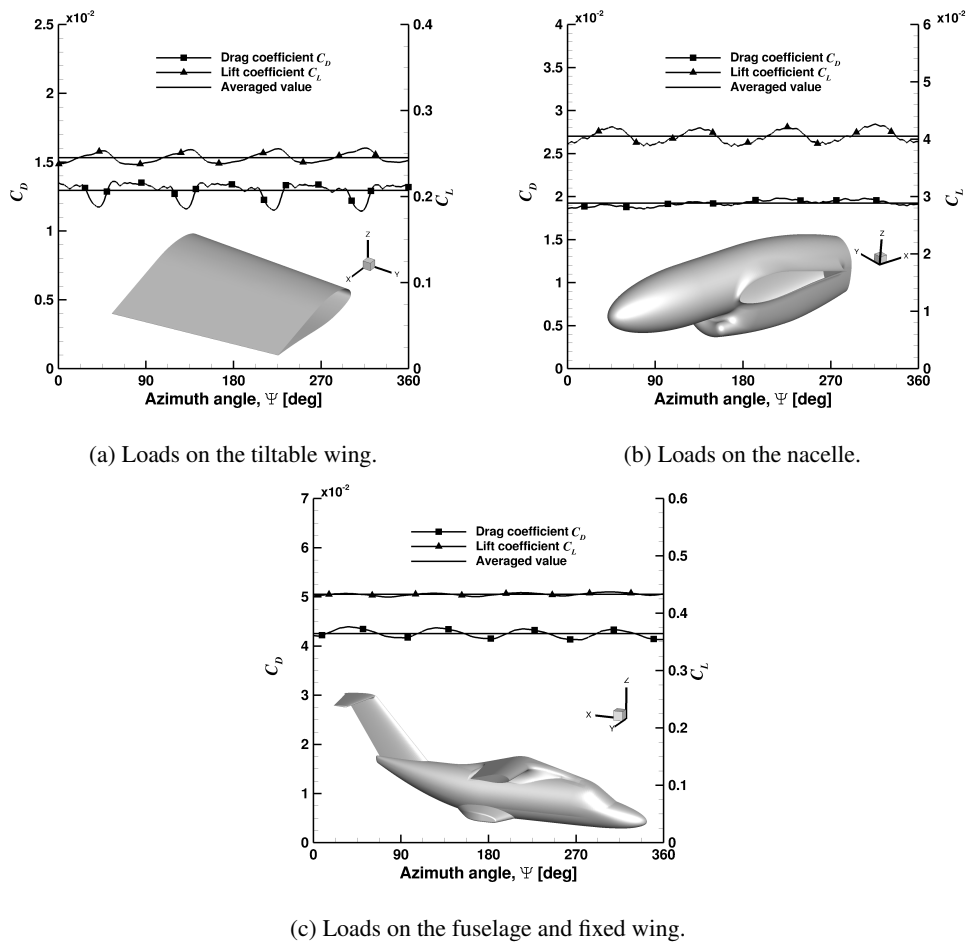
Fig. 12: History of the lift and drag coefficients in the tiltable wing, nacelle, and fuselage and fixed wing of the ERICA tiltrotor.
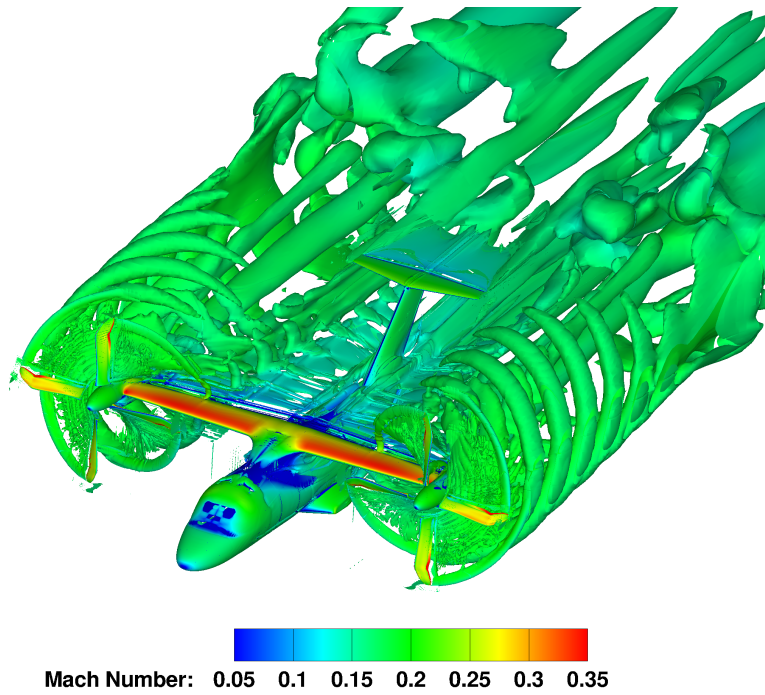
(a) Wake of the FRB solution.
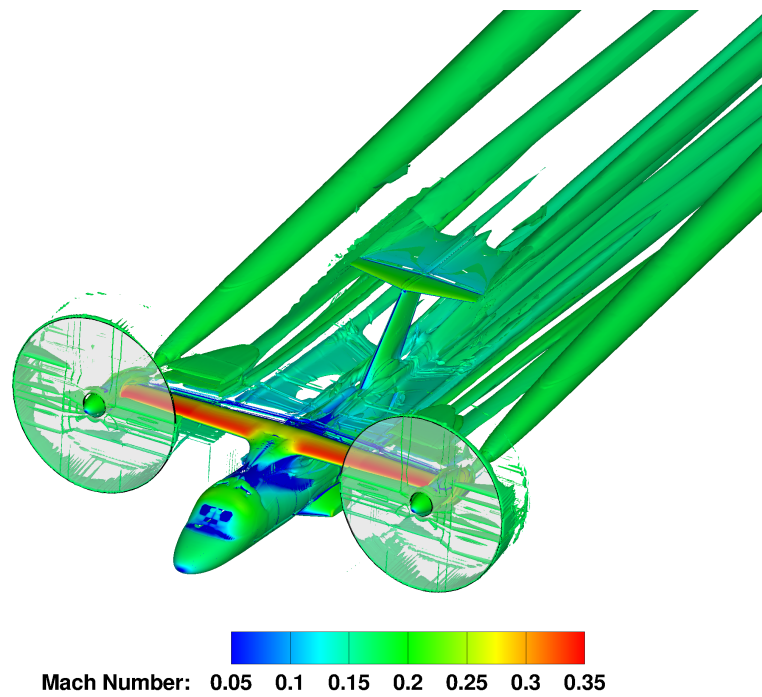
(b) Wake of the URAD solution.

Fig. 13: Wake-visualisation of the ERICA tiltrotor in aeroplane mode configuration using $\bar{Q}$-criterion ($\bar{Q}$=0.075) shaded by contour of Mach numbers. Results with the FRB (above) and URAD (below).
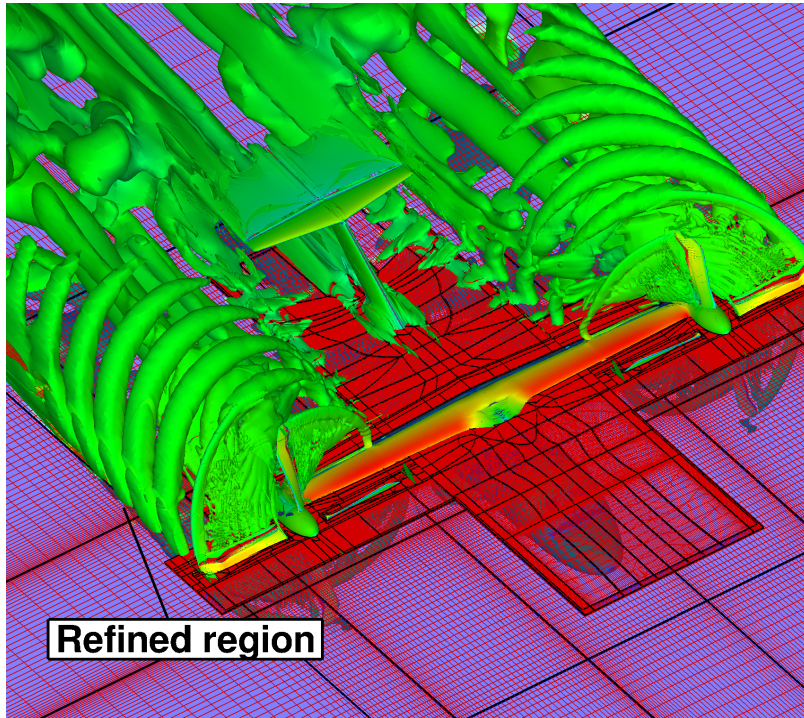
Fig. 14: Detailed view of the refined mesh employed for the aeroplane mode configuration with the fully resolved blade.
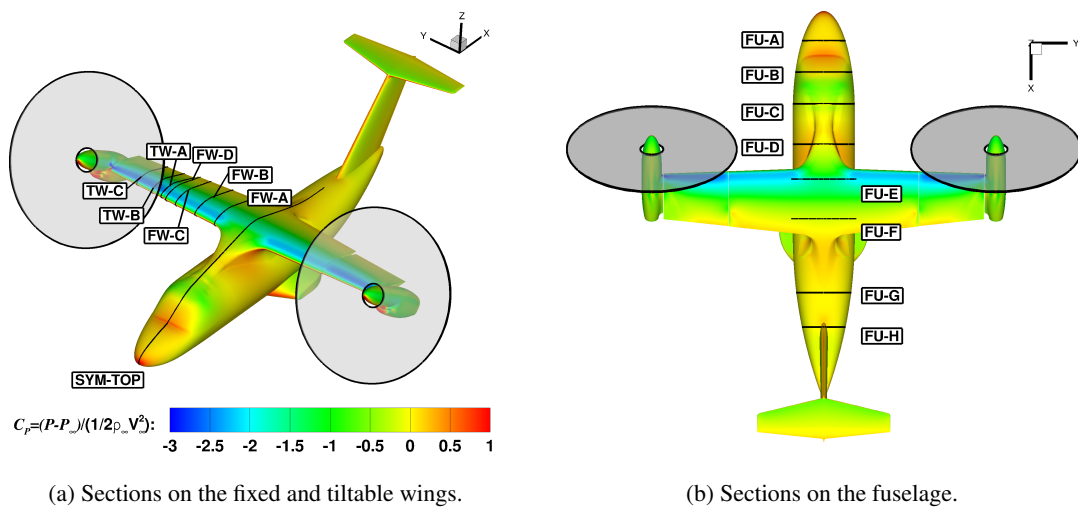
(a) Sections on the fixed and tiltable wings.

(b) Sections on the fuselage.

Fig. 15: Cross-sections selected for comparisons between CFD and experiments [11, 12] on the fixed and tiltable wings, and fuselage of the ERICA tiltrotor for the transition corridor configuration.
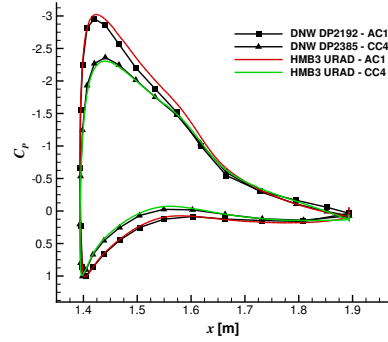
(a) SYM-TOP, section y=0 mm.

(b) FW-A, section y=280 mm.

(c) FW-B, section y=490 mm.

(d) FW-C, section y=700 mm.

(e) FW-D, section y=805 mm.

(f) TW-A, section y=855 mm.

(g) TW-B, section y=995 mm.

(h) TW-C, section y=1117 mm.

Fig. 16: C_P profile comparisons between CFD and experiments [11, 12] on the fixed and tiltable wings of the ERICA tiltrotor for the transition corridor configuration.

(a) FU-A, section x=260 mm.

(b) FU-B, section x=535 mm.

(c) FU-C, section x=810 mm.

(d) FU-D, section x=1163 mm.

(e) FU-E, section x=1470 mm.

(f) FU-F, section x=1810 mm.

(g) FU-G, section x=2460 mm.

(h) FU-H, section x=2760 mm.

Fig. 17: C_P profile comparisons between CFD and experiments [11, 12] on the fuselage of the ERICA tiltrotor for the transition corridor configuration.
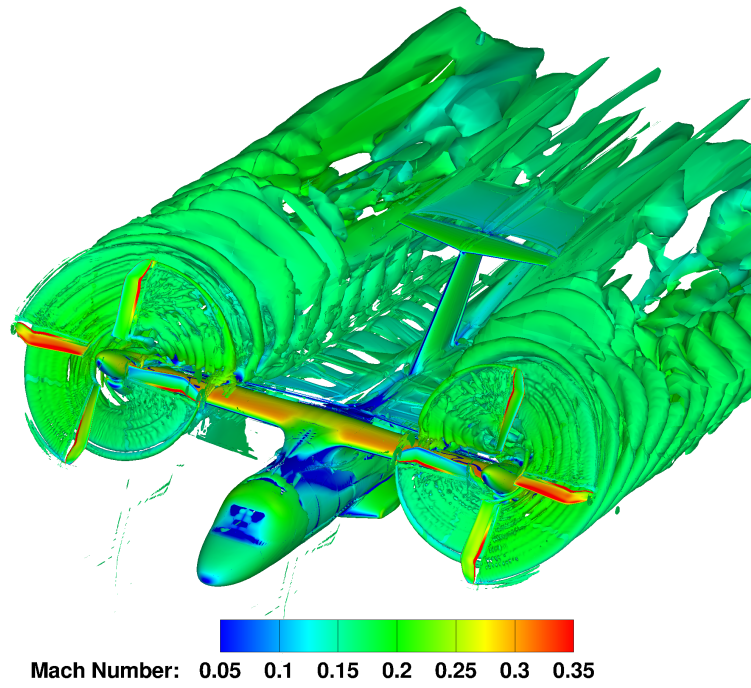
(a) Wake of the FRB solution.
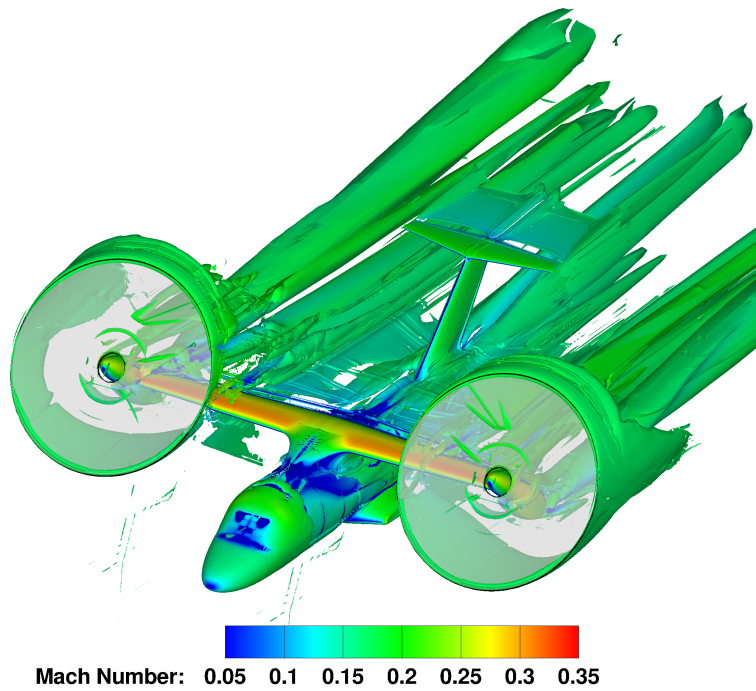
(b) Wake of the URAD solution.

Fig. 18: Wake-visualisation of the ERICA tiltrotor in transition corridor configuration using $\bar{Q}$-criterion ($\bar{Q}$=0.075) shaded by contour of Mach numbers. Results with the FRB (above) and URAD (below).
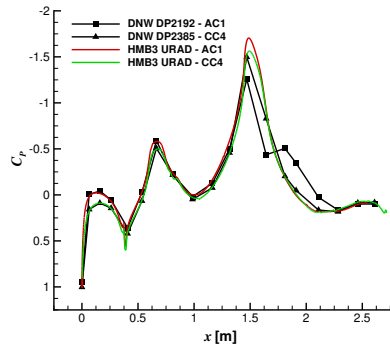
(a) SYM-TOP, section y=0 mm.
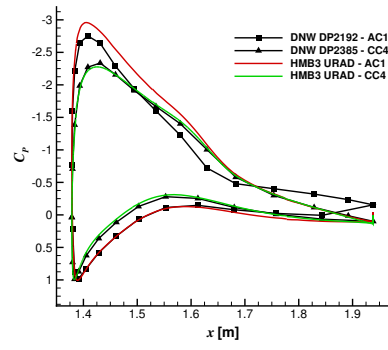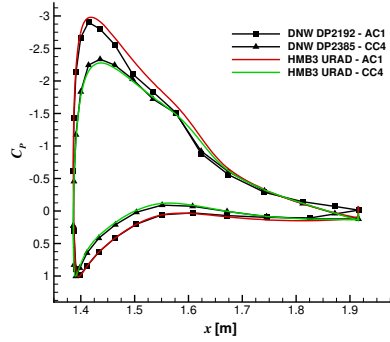
(b) FW-A, section y=280 mm.

(c) FW-B, section y=490 mm.

(d) FW-C, section y=700 mm.
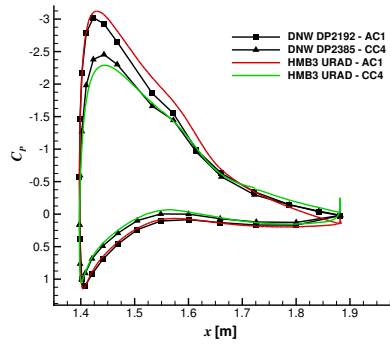
(e) FW-D, section y=805 mm.
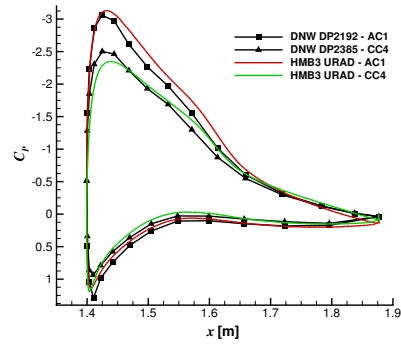
(f) TW-A, section y=855 mm.
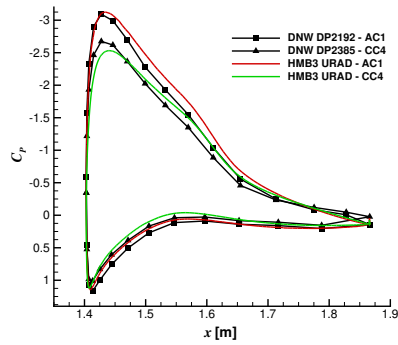
(g) TW-B, section y=995 mm.
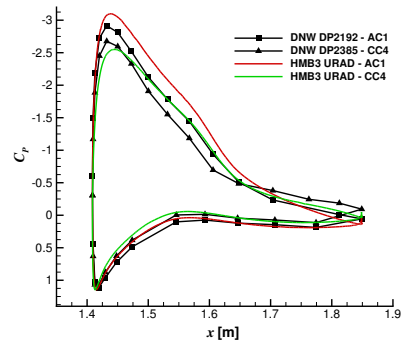
(h) TW-C, section y=1117 mm.

Fig. 19: C_P profile comparisons between CFD and experiments [11] on the fixed and tiltable wings of the ERICA tiltrotor for the aeroplane and transition corridor configurations.

C. Helicopter Mode HC3

1. C_P profile comparisons

Numerical simulations of a helicopter configuration (nacelles tilted 86.6 degrees) labelled as HC3 is also carried out. This configuration is characterised for a moderate forward speed ($M_\infty = 0.104$) with an aircraft angle of attack of -5.15 degrees (see Figure 5). Like the previous cases, profile comparisons of C_P between CFD and experiment were assessed on the fuselage, fixed and tiltable wing of the ERICA tiltrotor (see Figure 20) where a URAD approach was used. Unlike the AC1 and CC4 configurations where experiments in DNW and ONERA were available, the HC3 test was only carried out in the DNW wind tunnel.

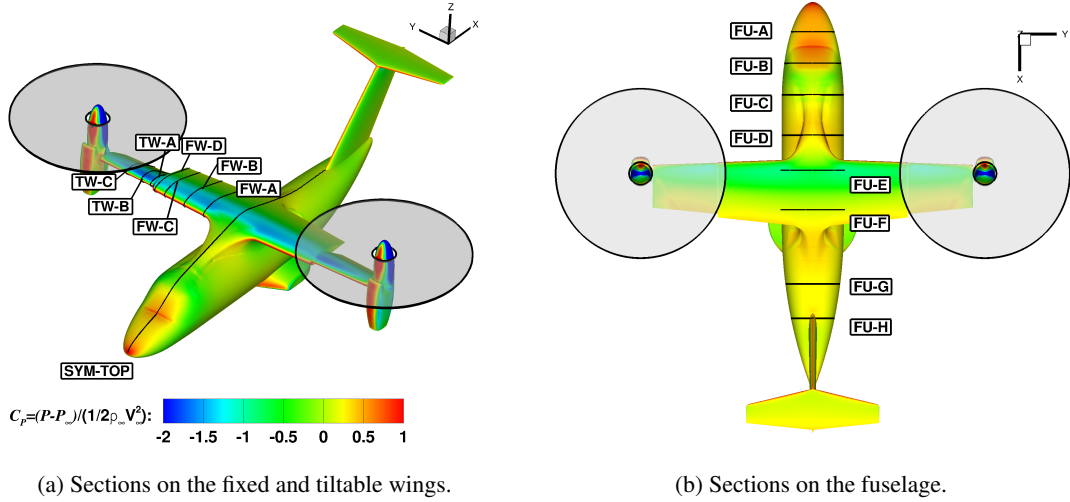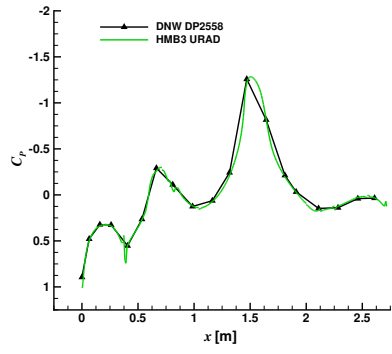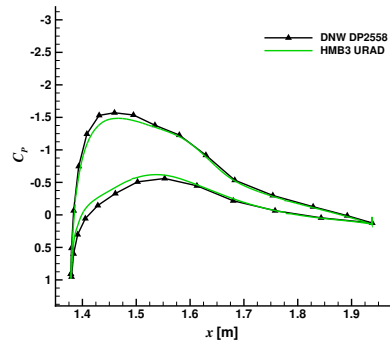(a) Sections on the fixed and tiltable wings.

(b) Sections on the fuselage.

Fig. 20: Cross-sections selected for comparisons between CFD and experiment [11] on the fixed and tiltable wings, and fuselage of the ERICA tiltrotor for the helicopter configuration.

Considering the pressure coefficient at the centre-line of the fuselage 21a, the DNW experiments suggest absence of flow separation. The CFD results are in a good agreement with experiments, and the suction peak is well represented ($C_{P\ HMB} = 1.28$; $C_{P\ DNW} = 1.26$) with a small discrepancy of 1.58%. The same analysis can be done for the inner fixed wing (see Figure 21b), where the suction peak and pressure plateau at the trailing edge are well captured. It is noticeable that discrepancies appear to be present, when sections on the fixed wing (Figures 21c-21f) are analysed. In fact, the CFD predictions reveal an under-predicted suction peak compared to the experiment, even if the pressure plateau distribution is well captured. The same behaviour was found at the aerodynamic interaction zone (Figures 21g-21d). It can be seen that experiments seem to predict separated flow at the further station on the tiltable wing (Figure 21d). The CFD predictions did not capture this the region of recirculation.

To conclude, the performance analysis of the ERICA tiltrotor for the HC3 configuration, a comparison of C_P profile have also been performed, considering eight cross-sections on the fuselage (Figures 22a-22h). As can be seen, all CFD curves are in close agreement with the experiments. This agreement is still fair for stations located behind the fixed wing and near the spoonsons (Figure 22f).
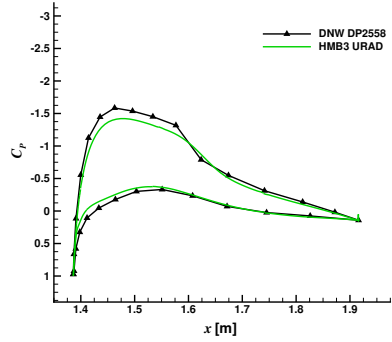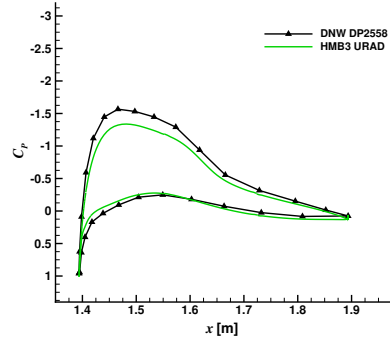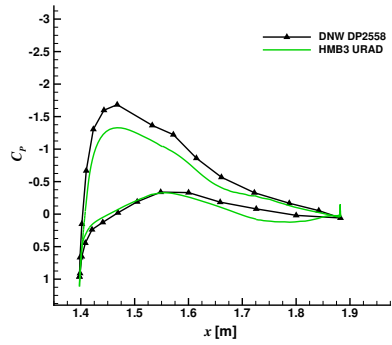
29

(a) SYM-TOP, section y=0 mm.
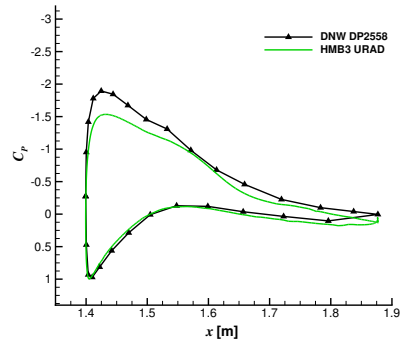
(b) FW-A, section y=280 mm.

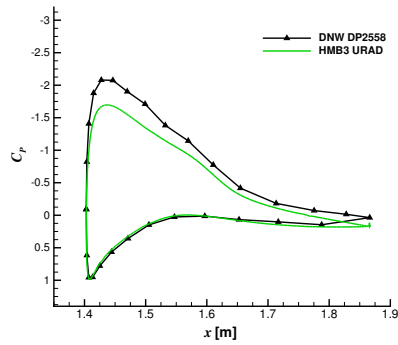(c) FW-B, section y=490 mm.

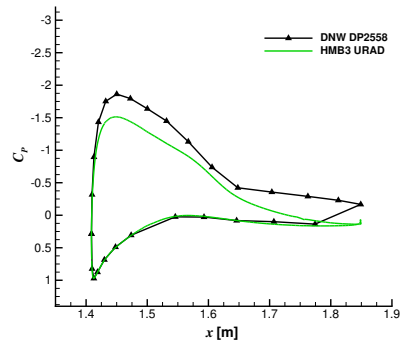(d) FW-C, section y=700 mm.

(e) FW-D, section y=805 mm.

(f) TW-A, section y=855 mm.

(g) TW-B, section y=995 mm.

(h) TW-C, section y=1117 mm.

Fig. 21: C_P profile comparisons between CFD and experiment [11] on the fixed and tiltable wings of the ERICA tiltrotor for the helicopter configuration.

(a) FU-A, section x=260 mm.

(b) FU-B, section x=535 mm.

(c) FU-C, section x=810 mm.

(d) FU-D, section x=1163 mm.

(e) FU-E, section x=1470 mm.

(f) FU-F, section x=1810 mm.

(g) FU-G, section x=2460 mm.
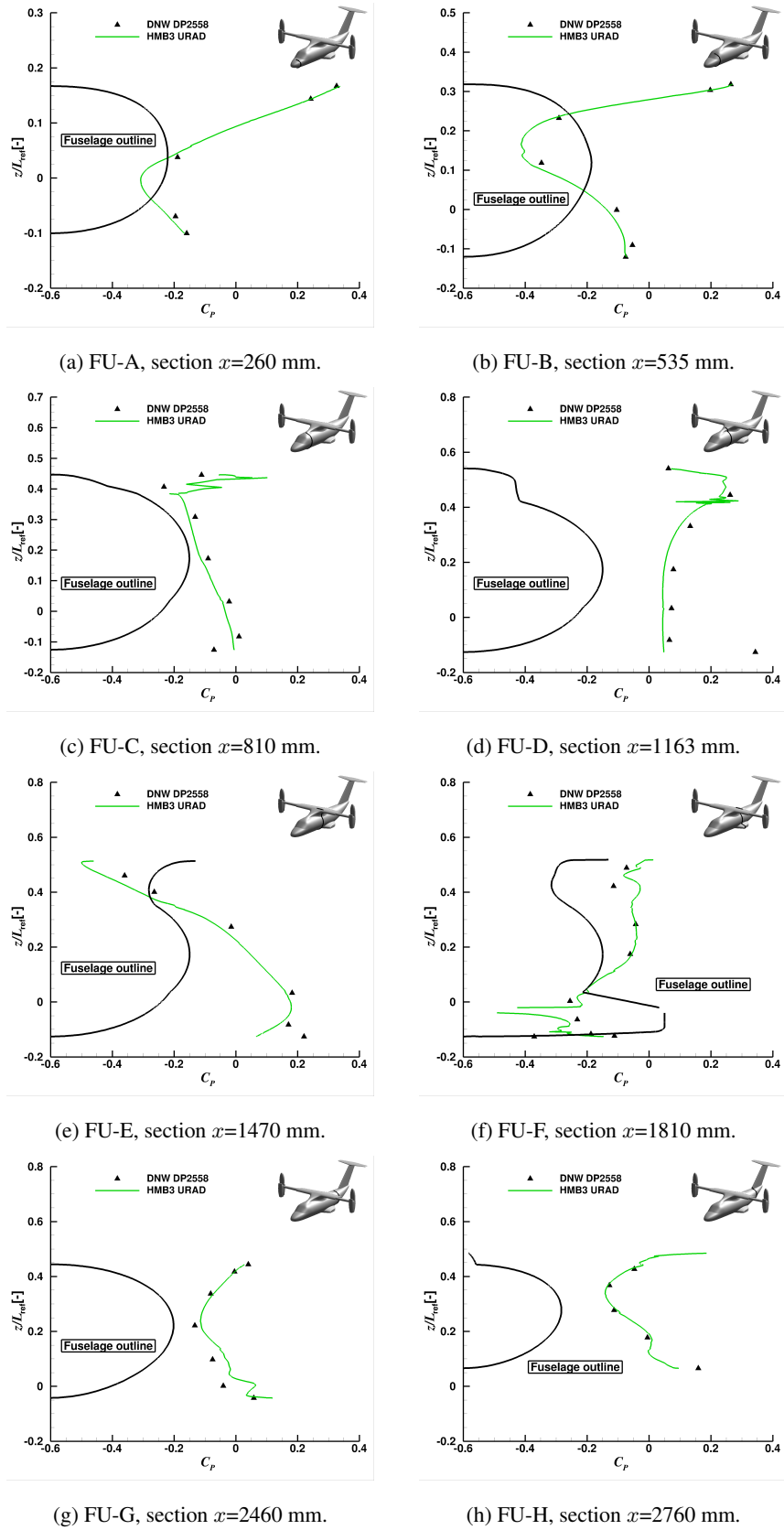
(h) FU-H, section x=2760 mm.

Fig. 22: C_P profile comparisons between CFD and experiment [11] on the fuselage of the ERICA tiltrotor for the helicopter configuration.

VI. Conclusions

This paper demonstrated the capability of CFD methods to predict tiltrotor flows. The 1:5 model-scale ERICA tiltrotor was considered for validation, where three flight configurations (aeroplane, transition corridor, and helicopter) were selected. The main conclusions are:

- The method was able to capture the fuselage surface pressure in different modes of flight.

- For the AC1 case, the aerodynamic interactions in the region of the nacelle and tiltable wing were captured by the FRB results, and the CFD with URAD and NURAD models also produced adequate estimates of the wing loads. The effect of the model support was also investigated and it was found that sting-mounted cases was less intrusive. The overall lift and drag of the vehicle were not, however, captured accurately.

- For the CC4 case, C_P comparisons between CFD and experiments showed good agreement for all stations investigated with small discrepancies between FRB and URAD results.

- Regarding the HC3 case, CFD results under-estimated the distribution of surface pressure coefficient at the aerodynamic interaction zone. The reason of this discrepancy may be due to lack of exact trimmed conditions. The presented results show clearly that computations with resolved blades are necessary if all flow details must be accurately captured.

[1] Maisel, M. D., Giulianetti, D. J., and Dugan, D. C., "The History of the XV-15 Tilt Rotor Research Aircraft: From Concept to Flight," NASA SP-2000-4517, 2000.

[2] Felker, F. F. and Light, J. S., "Rotor/Wing Aerodynamic Interactions in Hover," NASA-TM-88255, May 1986.

[3] Potsdam, M. A. and Strawn, R. C., "CFD Simulations of Tiltrotor Configurations in Hover," *Journal of the American Helicopter Society*, Vol. 50, No. 1, 2005, pp. 82–94, DOI: 10.4050/1.3092845.

[4] Bridgeman, J. O., Cummings, A., Narramore, J. C., and Kisor, R., "Analysis of V-22 Rotor Blade Performance Enhancements for Improved Payload," *Proceedings of the 64th American Helicopter Society Annual Forum*, AHS, Montreal, Canada, 2008, pp. 1–12.

[5] "Development of an advanced rotor for tilt-rotor," http://www.transport-research.info/project/development-advanced-rotor-tilt-rotor, last visited date: 29/09/2016.

[6] A. Visingardi, W. Khier, J. D., "The Blind-Test Activity of TILTAERO Project for the Numerical Aerodynamic Investigation of a Tilt Rotor," *Proceedings of the European Congress on Computational Methods in Applied Sciences and Engineering*, ECCOMAS, JyvÃd'skylÃd', Finland, 2004, pp. 1–20.

[7] Beaumier, P., Decours, J., and Lefebvre, T., "Aerodynamic and Aero-acoustic Design of Modern Tilt-rotors: The ONERA Experience," *Proceedings of the 26th International Congress of the Aeronautical Sciences*, ICAS, Anchorage, Alaska, 2008, pp. 1–11.

[8] Decours, J. and Lefebvre, T., "Navier-Stokes computations applied to tilt-rotors," *Proceedings of the 33rd European Rotorcraft Forum*, ERF, Kazan, Russia, 2007, pp. 1–18.

[9] "NICETRIP - Novel Innovative Competitive Effective Tilt Rotor Integrated Project: NICETRIP website," http://www.transport-research.info/project/novel-innovative-competitive-effective-tilt-rotor-integrated-project, last visited date: 29/09/2016.

[10] Alli, P., Nannoni, F., and Cicalé, M., "ERICA: The European Tiltrotor Design and Critical Technology Projects," *AIAA/ICAS, International Air and Scpace Symposium and Exposition: The Next 100 Years*, Day-ton, Ohio, USA, 2005.

[11] Philipsen, I. and Heinrich, S., "Test Report on Measurements on the NICETRIP Large-Scale Powered Model in DNW-LLF," Project number 2410.1338, Aug. 2013.

[12] Lebrun, F., "NICETRIP test - ERICA 1/5th scale powered model in the test section no.2 - $45m^2$ of S1MA wind tunnel," Test Report Number PV 1/17648 DSMA, June 2014.

[13] Gates, S., "Aerodynamic Analysis of Tiltrotors in Hovering and Propeller Modes Using Advanced Navier-Stokes Computations," *Proceedings of the Thirty-Nineth European Rotorcraft Forum*, ERF, Moscow, Russia, 2013, pp. 1–26.

[14] Anon, "Advancement of Proprotor Technology Task II - Wind Tunnel Results," NASA CR–114363, Sept. 1971.

[15] Felker, F. F., Betzina, M. D., and Signor, D. B., "Performance and Loads Data from a Hover Test of a Full-Scale XV-15 Rotor," NASA TM–86833, Sept. 1985.

[16] Betzina, M. D., "Rotor Performance of an Isolated Full-Scale XV-15 Tiltrotor in Helicopter Mode," *Proceedings of the American Helicopter Society Aerodynamics, Acoustics, and Test and Evaluation Technical Specialist Meeting*,

AHS, San Francisco, CA, 2002, pp. 1–12.

[17] Lefebvre, T., Beaumier, P., Canard, S., Pisoni, A., Pagano, A., van der Wall, B., D'Alascio, A., Arzoumanian, C., Riziotis, V., and Hermans, C., "Aerodynamic and Aero-acoustic Optimization of Modern Tilt-Rotor Blades within the ADYN Project," *Proceedings of the European Congress on Computational Methods in Applied Sciences and Engineering*, ECCOMAS, JyvÃd'skylÃd', Finland, 2004, pp. 1–20.

[18] Fox, E., "BVWT 0468 - 0.15 Scale V-22 High Angle of Attack Wind Tunnel Test Report," Boeing Document Number 901-909-665, Feb. 2000.

[19] Abras, J. and Narducci, R., "Analysis of CFD Modeling Techniques over the MV-22 Tiltrotor," *Proceedings of the 66th Annual Forum*, AHS, Phoenix, AZ, 2010, pp. 1–11.

[20] Decours, J., Beaumier, P., Khier, W., Kneisch, T., Valentini, M., and Vigevano, L., "Experimental Validation of Tilt-Rotor Aerodynamic Predictions," *Proceeding of the 40th European Rotorcraft Forum*, ERF, Southampton, UK, 2014, pp. 1–12.

[21] Barakos, G., Steijl, R., Badcock, K., and Brocklehurst, A., "Development of CFD Capability for Full Helicopter Engineering Analysis," *Proceedings of the 31st European Rotorcraft Forum*, ERF, Florence, Italy, 2005, pp. 1–15.

[22] Hirt, C. W., Amsten, A. A., and Cook, J. L., "An Arbitrary Lagrangian-Eulerian Computing Method for All Flow Speeds," *Journal of Computational Physics*, Vol. 14, No. 3, 1974, pp. 227–253, DOI: 10.1006/jcph.1997.5702.

[23] Osher, S. and Chakravarthy, S., "Upwind schemes and boundary conditions with applications to Euler equations in general geometries," *Journal of Computational Physics*, Vol. 50, No. 3, 1983, pp. 447–481, DOI: 10.1016/0021-9991(83)90106-7.

[24] Roe, P. L., "Approximate Riemann Solvers, Parameter Vectors, and Difference Schemes," *Journal of Computational Physics*, Vol. 43, No. 2, 1981, pp. 357–372, DOI: 10.1016/0021-9991(81)90128-5.

[25] van Leer, B., "Towards the ultimate conservative difference scheme. V.A second-order sequel to Godunov's Method," *Journal of Computational Physics*, Vol. 32, No. 1, 1979, pp. 101–136, DOI: 10.1016/0021-9991(79)90145-1.

[26] van Albada, G. D., van Leer, B., and Roberts, W. W., "A Comparative Study of Computational Methods in Cosmic Gas Dynamics," *Astronomy and Astrophysics*, Vol. 108, No. 1, 1982, pp. 76–84.

[27] Axelsson, O., *Iterative Solution Methods*, Cambridge University Press: Cambridge, MA, 1994.

[28] Jameson, A., Schmidt, W., and Turkel, E., "Numerical Solutions of Euler Equations by Finite Volume Methods Using Runge-Kutta Time-Stepping Schemes," *Proceedings of the 14th Fluid and Plasma Dynamic Conference*, AIAA, Palo Alto, California, 1981, pp. 1–19.

[29] Steijl, R. and Barakos, G. N., "Sliding mesh algorithm for CFD analysis of helicopter rotor-fuselage aerodynamics," *International Journal for Numerical Methods in Fluids*, Vol. 58, No. 5, 2008, pp. 527–549, DOI: 10.1002/d.1757.

[30] Jarkowski, M., Woodgate, M., Barakos, G. N., and Rokicki, J., "Towards consistent hybrid overset mesh methods for rotorcraft CFD," *International Journal for Numerical Methods in Fluids*, Vol. 74, No. 8, 2014, pp. 543–576, DOI: 10.1002/fld.3861.

[31] Dehaeze, F. and Barakos, G. N., "Aeroelastic CFD Computations for Rotor Flows," *Proceedings of the 37th European Rotorcraft Forum*, ERF, Galarate, Italy, 2011, pp. 1–20.

[32] Jimenez, A. and Barakos, G. N., "Hover Predictions on the S-76 Rotor using HMB2," *Proceedings of the 53rd Aerospace Sciences Meeting*, AIAA, Kissimmee, Florida, 2015, pp. 1–34.

[33] Leishman, J. G., *Principles of Helicopter Aerodynamics*, Cambridge University Press, 2006.

[34] Shaidakov, V. I., "Disc Vortex Theory of the Main Rotor with the Constant Load over a Disc," *Proektirovanie vertoletov (Helicopter Design), Moscow: MAI*, Vol. 381, 1976.

[35] Crozon, C., *Coupling Flight Mechanics and CFD Numerical Simulation of Shipborne Rotors*, Ph.D. thesis, Univer-

sity of Liverpool, UK, June 2015.

[36] Bruin, A. and Schneider, O., "A Discussion of Measured Static and Dynamic Rotor Loads During Testing of the ER-ICA Tilt-Wing Rotorcraft Configuration in DNW-LLF Wind Tunnel," *Proceeding of the 40th European Rotorcraft Forum*, ERF, Southampton, UK, 2014, pp. 1–15.

[37] Vigevano, L., Beaumier, P., Decours, J., Khier, W., Kneisch, T., and Vitagliano, P., "Tilt-Rotor Aerodynamics Activities During the NICETRIP Project," *Proceeding of the 40th European Rotorcraft Forum*, ERF, Southampton, UK, 2014, pp. 1–14.

[38] Wilcox, D., "Reassessment of the scale-determining equation for advacned turbulence models," *AIAA journal*, Vol. 26, No. 11, 1988, pp. 1299–1310, DOI: 10.2514/3.10041.

[39] Jeong, J. and Hussain, F., "On the identification of a vortex," *Journal of Fluid Mechanics*, Vol. 285, 1995, pp. 69–94, DOI: 10.1017/S0022112095000462.